Investigation of nonequilibrium effects across normal shock waves by means of a spectral-Lagrangian Boltzmann solver

Alessandro Munafò*

Aeronautics and Aerospace Department, von Karman Institute for Fluid Dynamics, Belgium

Erik Torres†

Aeronautics and Aerospace Department, von Karman Institute for Fluid Dynamics, Belgium

Jeffrey R. Haack‡

Department of Mathematics, The University of Texas at Austin, TX

Irene M. Gamba§

ICES and Department of Mathematics, The University of Texas at Austin, TX

Thierry E. Magin¶

Aeronautics and Aerospace Department, von Karman Institute for Fluid Dynamics, Belgium

A spectral-Lagrangian deterministic solver for the Boltzmann equation for rarefied gas flows is proposed. Numerical solutions are obtained for the flow across normal shock waves of pure gases and mixtures by means of a time-marching method. Operator splitting is used. The solution update is obtained as a combination of the operators for the advection (or transport) and homogeneous (or collision) problems. For the advection problem, the Finite volume method is considered. For the homogeneous problem, a spectral-Lagrangian numerical method is used. The latter is based on the weak form of the collision operator and can be used with any type of cross-section model. The conservation of mass, momentum and energy during collisions is enforced through the solution of a constrained optimization problem. Numerical results are compared with those obtained by means of the DSMC method. Very good agreement is found for the whole range of free-stream Mach numbers being considered. For the pure gas case, a comparison with experimentally acquired density profiles is also performed, allowing for a validation of the spectral-Lagrangian solver.

*PhD. candidate, Aeronautics/Aerospace department, von Karman Institute for Fluid Dynamics, Chaussée de Waterloo 72, 1640 Rhode-Saint-Genèse, Belgium, AIAA member, munafo@vki.ac.be.

†PhD. candidate, Aeronautics/Aerospace department, von Karman Institute for Fluid Dynamics, Chaussée de Waterloo 72, 1640 Rhode-Saint-Genèse, Belgium, AIAA member, torres@vki.ac.be.

‡Post-doctoral fellow, Department of Mathematics, 1 University Station C2000, University of Texas at Austin, Austin, TX 78712. haack@math.utexas.edu.

§Professor of Mathematics, The Institute for Computational Engineering and Sciences (ICES) and Department of Mathematics, 1 University Station C2000, University of Texas at Austin, Austin, TX 78712, gamba@math.utexas.edu.

¶Associate professor, Aeronautics/Aerospace department, von Karman Institute for fluid dynamics, Chaussée de Waterloo 72, 1640 Rhode-Saint-Genèse, Belgium, AIAA member, magin@vki.ac.be.

I. Introduction

Possible applications of rarefied gas dynamics include the computation of the flowfield around spacecraft entering planetary atmospheres and the flow in hypersonic wind tunnels. Understanding rarefied gas effects in aerospace applications is important for an accurate calculation of the aerodynamic coefficients during the early phase of the entry of a space capsule into a planetary atmosphere, prediction of the heat flux experienced by ballutes during entry and descent, and also a correct interpretation of experimental measurements.

Attempts to compute rarefied flows by means of a hydrodynamic description based on the Navier-Stokes equations give inaccurate results due to the failure of Newton's law for the stress tensor and Fourier's law for the heat flux vector in the rarefied regime [1, 2].

The Boltzmann equation provides a statistical description of dilute gaseous systems valid from the rarefied to the hydrodynamic regime [1, 2]. It describes the evolution of the species distribution function in the phase-space. Once the distribution function of each species known, it is possible to compute macroscopic observables such as density, hydrodynamic velocity and temperature by means of suitable moments. The computation of numerical solutions of the Boltzmann equation is not trivial. This is due to the integro-differential nature of the equation. A further source of difficulty is the high dimensionality of the problem (numerical solutions must be sought in the phase-space). Stochastic-like solutions of the Boltzmann equation can be obtained by means of the Direct-Simulation-Monte-Carlo (DSMC) method [3, 4]. The former is a particle-based technique and has proven to be accurate [4]. However, it shares the drawbacks of stochastic methods, the main one being the presence of noise in the numerical results [3]. The former problem affects, in particular, the accuracy of the solution for low speed and unsteady flows. Parallel to the development of the DSMC method, deterministic numerical methods for the Boltzmann equation have been proposed. These comprise, among all, discrete velocity models [5, 6] and spectral methods [7, 8]. The main advantage of a deterministic method over the DSMC technique is that the numerical solution obtained is not affected by numerical noise. Deterministic methods can also be applied to flow problems in the hydrodynamic and transition regime, for which the use of the DSMC method becomes prohibitively expensive [9].

In the present work, an already existing spectral-Lagrangian solver for the Boltzmann equation for hard-sphere gases [7, 10] is extended in order to deal with gas mixtures and account for more realistic collision cross-section models. Numerical solutions of the Boltzmann equation are obtained for the flow across normal shock waves of pure gases and mixtures. The key-part of the spectral-Lagrangian Boltzmann solver is the computational algorithm for the evaluation of the collision operator. The former is based on the weak form of the latter and can be used with any type of cross-section model. The conservation of mass, momentum and energy during collisions is enforced through the solution of a constrained optimization problem. Despite the formulation for internal energy excitation and relaxation is included in the numerical method, computational results are only shown for pure and mixture of monatomic gases.

The purpose of the paper consists in the verification and validation of the spectral-Lagrangian Boltzmann solver through comparison with DSMC and experimental results, respectively.

The paper is structured as follows. Section II introduces the physical model. The numerical method is described in detail in Sect. III. Computational results are presented and discussed in Sect. IV. Conclusions are outlined Sect. V.

II. Physical modeling

II.A. Simplifying assumptions and conventions

The physical model used in the present work is based on the following assumptions and conventions [11]:

1. The gas mixture is composed of identical particles.
2. Particles have discrete internal energy levels:
   - The indices of energy levels are stored in the set $\mathcal{I}_{\mathcal{S}} = \{1, \ldots, N_s\}$, N_s being the number of species.
   - The mass of the species (energy level) $i \in \mathcal{I}_{\mathcal{S}}$ is m_i.
   - The degeneracy and the energy of the energy level $i \in \mathcal{I}_{\mathcal{S}}$ are g_i and E_i, respectively.
3. Only binary collisions are accounted for:

$$i + j = i' + j', \quad i, j, i', j' \in \mathcal{I}_{\mathcal{S}}. \tag{1}$$

- Elastic collision: $i = i'$ and $j = j'$.
- Inelastic collision: $(i', j, j') \in \mathcal{C}_i^{\text{in}}$. The set $\mathcal{C}_i^{\text{in}}$ stores the ordered triplets (i', j, j') for all the possible inelastic collisions involving the species i as reactant in Eq. (1) and is defined as:

$$\mathcal{C}_i^{\text{in}} = \left\{ (i', j, j') \in \left[\mathcal{I}_\mathcal{S} \,\mathrm{x}\, \mathcal{I}_\mathcal{S} \,\mathrm{x}\, \mathcal{I}_\mathcal{S} \setminus \bigcup_{s \in \mathcal{I}_\mathcal{S}} (i, s, s) \right] \right\}, \quad i \in \mathcal{I}_\mathcal{S}. \tag{2}$$

4. The presence of chemical reactions (such as dissociation and ionization) and external force fields is neglected.

II.B. The Boltzmann equation

Based on the hypothesis introduced in the Sect. II.A, a Boltzmann equation can be written for the velocity distribution function $f_i(\mathbf{x}, \mathbf{v}, t)$ of the species $i \in \mathcal{I}_\mathcal{S}$:

$$\frac{\partial f_i}{\partial t} + \mathbf{v} \cdot \frac{\partial f_i}{\partial \mathbf{x}} = \sum_{j \in \mathcal{I}_\mathcal{S}} Q_{ij}(\mathbf{v}) + \sum_{(i', j, j') \in \mathcal{C}_i^{\text{in}}} Q_{ij}^{i'j'}(\mathbf{v}), \quad i \in \mathcal{I}_\mathcal{S}. \tag{3}$$

In Eq. (3) the quantities $Q_{ij}(\mathbf{v})$ and $Q_{ij}^{i'j'}(\mathbf{v})$ are, respectively, the elastic and inelastic collision operators [1]:

$$Q_{ij}(\mathbf{v}) = \iint\limits_{\substack{\mathbf{w} \in \Re^3, \\ \omega' \in S^2}} \left[f_i(\mathbf{v}') \, f_j(\mathbf{w}') - f_i(\mathbf{v}) \, f_j(\mathbf{w}) \right] \sigma_{ij} \, u \, d\omega' \, d\mathbf{w}, \quad i, j \in \mathcal{I}_\mathcal{S}, \tag{4}$$

$$Q_{ij}^{i'j'}(\mathbf{v}) = \iint\limits_{\substack{\mathbf{w} \in \Re^3, \\ \omega' \in S^2}} \left[\frac{g_i \, g_j}{g_{i'} \, g_{j'}} f_{i'}(\mathbf{v}') \, f_{j'}(\mathbf{w}') - f_i(\mathbf{v}) \, f_j(\mathbf{w}) \right] \sigma_{ij}^{i'j'} \, u \, d\omega' \, d\mathbf{w}, \quad i \in \mathcal{I}_\mathcal{S}, \, (i', j, j') \in \mathcal{C}_i^{\text{in}}. \tag{5}$$

In Eqs. (4) - (5), $\mathbf{v}$ and $\mathbf{w}$ are, respectively, the velocities of the species i and j, u is the relative velocity magnitude $u = |\mathbf{v} - \mathbf{w}|$, ω' is the solid angle of the scattering direction, and σ_{ij} and $\sigma_{ij}^{i'j'}$ are, respectively, the differential cross-sections for the elastic and inelastic collision associated to the binary interaction given in Eq. (1). It is important to mention that the potential model used to obtain the differential cross-section is general and not restricted to hard-sphere interactions. As usual, primed variables in Eqs. (4) - (5) (and in what follows) refer to post-collisional values. Their values are related to pre-collisional values through the conservation of momentum and energy:

$$m_i \, \mathbf{v} + m_j \, \mathbf{w} = m_{i'} \, \mathbf{v}' + m_{j'} \, \mathbf{w}', \tag{6}$$

$$\frac{1}{2} m_i \, v^2 + E_i + \frac{1}{2} m_j \, w^2 + E_j = \frac{1}{2} m_{i'} \, v'^2 + E_{i'} + \frac{1}{2} m_{j'} \, w'^2 + E_{j'}, \quad i, j, i', j' \in \mathcal{I}_\mathcal{S}. \tag{7}$$

Note that for a pure gas with internal energy the mass of all the particles are identical ($m_i = m_j = m_{i'} = m_{j'}$).

Eq. (3) may also be used for the case of a mixture of monatomic gases without internal energy. In this situation, $m_i = m_{i'}$ and $m_j = m_{j'}$. Moreover only elastic collisions occur and all the terms $Q_{ij}^{i'j'}(\mathbf{v})$ in Eq. (3) are zero.

II.C. The Fourier transform of the elastic and inelastic collision operators

The numerical method in use in the present work (see Sect. III) makes use of the Fourier transform of the elastic and inelastic collision operators [12] (Eqs. (4) - (5), respectively). The former can be computed based on their weak form:

$$\int\limits_{\mathbf{v} \in \Re^3} \Phi_i(\mathbf{v}) \, Q_{ij}(\mathbf{v}) \, d\mathbf{v} = \iiint\limits_{\substack{\mathbf{w} \in \Re^3, \mathbf{v} \in \Re^3, \\ \omega' \in S^2}} f_i(\mathbf{v}) \, f_j(\mathbf{w}) \left[\Phi_i(\mathbf{v}') - \Phi_i(\mathbf{v}) \right] \sigma_{ij} \, u \, d\omega' \, d\mathbf{w} \, d\mathbf{v}, \quad i, j \in \mathcal{I}_\mathcal{S}, \tag{8}$$

$$\int\limits_{\mathbf{v} \in \Re^3} \Phi_i(\mathbf{v}) \, Q_{ij}^{i'j'}(\mathbf{v}) \, d\mathbf{v} = \iiint\limits_{\substack{\mathbf{w} \in \Re^3, \mathbf{v} \in \Re^3, \\ \omega' \in S^2}} f_i(\mathbf{v}) \, f_j(\mathbf{w}) \left[\Phi_{i'}(\mathbf{v}') - \Phi_i(\mathbf{v}) \right] \sigma_{ij}^{i'j'} \, u \, d\omega' \, d\mathbf{w} \, d\mathbf{v}, \quad i \in \mathcal{I}_\mathcal{S}, (i', j, j') \in \mathcal{C}_i^{\text{in}}, \tag{9}$$

where the function $\Phi_i(\mathbf{v})$ in Eqs. (8) - (9) is a smooth test function of the velocity $\mathbf{v}$. The substitution of a Fourier velocity mode $\Phi_i(\mathbf{v}) = (2\pi)^{-3/2} \exp(-\imath\, \boldsymbol{\zeta} \cdot \mathbf{v})$ in Eqs. (8) - (9) gives the Fourier transform of the elastic and inelastic collision operators and, after some algebraic manipulation (similar to [7]), the following expressions are obtained:

$$\hat{Q}_{\,ij}(\boldsymbol{\zeta}) = \frac{1}{\left(\sqrt{2\,\pi}\right)^3} \int\limits_{\boldsymbol{\xi} \in \Re^{\,3}} \hat{f}_i\,(\boldsymbol{\zeta} - \boldsymbol{\xi})\;\hat{f}_j(\boldsymbol{\xi})\,\tilde{G}_{ij}\,(\boldsymbol{\zeta}, \boldsymbol{\xi})\;d\boldsymbol{\xi}, \quad i, j \in \mathcal{I}_{\mathcal{S}}, \tag{10}$$

$$\hat{Q}_{ij}^{\,i'j'}(\boldsymbol{\zeta}) = \frac{1}{\left(\sqrt{2\,\pi}\right)^3} \int\limits_{\boldsymbol{\xi} \in \Re^{\,3}} \hat{f}_i\,(\boldsymbol{\zeta} - \boldsymbol{\xi})\;\hat{f}_j(\boldsymbol{\xi})\,\tilde{G}_{ij}^{\,i'j'}\,(\boldsymbol{\zeta}, \boldsymbol{\xi})\;d\boldsymbol{\xi}, \quad i \in \mathcal{I}_{\mathcal{S}},\; (i', j, j') \in \mathcal{C}_i^{\,\mathrm{in}}. \tag{11}$$

In Eqs. (10) - (11), the quantities $\hat{f}_i$ and $\hat{f}_j$ are, respectively, the Fourier transform of the distribution functions of the species i and j, while the quantities $\tilde{G}_{ij}\,(\boldsymbol{\zeta}, \boldsymbol{\xi})$ and $\tilde{G}_{ij}^{\,i'j'}\,(\boldsymbol{\zeta}, \boldsymbol{\xi})$ are weight functions defined as:

$$\tilde{G}_{ij}\,(\boldsymbol{\zeta}, \boldsymbol{\xi}) = \iint\limits_{\substack{\mathbf{u} \in \Re^{\,3}, \\ \omega' \in S^{\,2}}} u\,\sigma_{ij}\,\left\{\exp\left[-\imath\,\frac{\mu_{ij}}{m_i}\boldsymbol{\zeta} \cdot (\mathbf{u}' - \mathbf{u})\right] - 1\right\} \exp\left(-\imath\,\boldsymbol{\xi} \cdot \mathbf{u}\right)\,d\omega'\,d\mathbf{u}, \quad i, j \in \mathcal{I}_{\mathcal{S}}, \tag{12}$$

$$\tilde{G}_{ij}^{\,i'j'}\,(\boldsymbol{\zeta}, \boldsymbol{\xi}) = \iint\limits_{\substack{\mathbf{u} \in \Re^{\,3}, \\ \omega' \in S^{\,2}}} u\,\sigma_{ij}^{\,i'j'}\,\left\{\exp\left[-\imath\,\frac{\mu_{ij}}{m_i}\boldsymbol{\zeta} \cdot (\mathbf{u}' - \mathbf{u})\right] - 1\right\} \exp\left(-\imath\,\boldsymbol{\xi} \cdot \mathbf{u}\right)\,d\omega'\,d\mathbf{u}, \quad i \in \mathcal{I}_{\mathcal{S}},\; (i', j, j') \in \mathcal{C}_i^{\,\mathrm{in}}. \tag{13}$$

In Eqs. (12) - (13) the quantity $\mu_{ij} = m_i\,m_j/(m_i + m_j)$ is the reduced mass of the species i and j. From Eqs. (10) - (13), the following observations can be made:

1. The Fourier transform of the elastic and inelastic collision operators can be written as weighted convolutions in the Fourier velocity space, the weights being the functions $\tilde{G}_{ij}\,(\boldsymbol{\zeta}, \boldsymbol{\xi})$ and $\tilde{G}_{ij}^{\,i'j'}\,(\boldsymbol{\zeta}, \boldsymbol{\xi})$, respectively [7].

2. The weight functions $\tilde{G}_{ij}\,(\boldsymbol{\zeta}, \boldsymbol{\xi})$ and $\tilde{G}_{ij}^{\,i'j'}\,(\boldsymbol{\zeta}, \boldsymbol{\xi})$ depend only on the cross-section model in use. No dependence on the value of the species distribution function occurs. This fact can be exploited by a computational method (see Sect. III) that makes use of Eqs. (10) - (11) for the numerical evaluation of the elastic and inelastic collision operators (the weight associated to each interaction can be precomputed [13]).

3. Since in the definition provided by Eqs. (12) - (13) no assumption is done on the differential cross-section model, anisotropic interactions can also be taken into account [14].

In the case of a collision cross-section depending only on the relative velocity magnitude (isotropic interaction), the expression for the convolution weights in Eqs. (10) - (13) reduce to one-dimensional integrals:

$$\tilde{G}_{ij}\,(\boldsymbol{\zeta}, \boldsymbol{\xi}) = 16\,\pi^{\,2} \int\limits_{u \in [0, +\infty)} u^{\,3}\,\sigma_{ij}\,\left[\mathrm{sinc}\left(||\boldsymbol{\zeta}||_2\,\frac{\mu_{ij}}{m_i}\,u\right)\mathrm{sinc}\left(\left|\left|\boldsymbol{\xi} - \boldsymbol{\zeta}\,\frac{\mu_{ij}}{m_i}\right|\right|_2 u\right) - \mathrm{sinc}\left(||\boldsymbol{\xi}||_2\,u\right)\right] du, \quad i, j \in \mathcal{I}_{\mathcal{S}}, \tag{14}$$

$$\tilde{G}_{ij}^{\,i'j'}\,(\boldsymbol{\zeta}, \boldsymbol{\xi}) = 16\,\pi^{\,2} \int\limits_{u \in (u_{ij}^{\,i'j'}, +\infty)} u^3\,\sigma_{ij}^{\,i'j'}\,\left[\mathrm{sinc}\left(||\boldsymbol{\zeta}||_2\,\frac{\mu_{ij}}{m_i}\,u\,\beta_{ij}^{\,i'j'}\right)\mathrm{sinc}\left(\left|\left|\boldsymbol{\xi} - \boldsymbol{\zeta}\frac{\mu_{ij}}{m_i}\right|\right|_2 u\right) - \mathrm{sinc}\left(||\boldsymbol{\xi}||_2\,u\right)\right] du,$$
$$i \in \mathcal{I}_{\mathcal{S}},\; (i', j, j') \in \mathcal{C}_i^{\,\mathrm{in}}. \tag{15}$$

In Eqs. (14)-(15), the symbol $||\,||_2$ stands for the L_2 norm and the threshold relative velocity magnitude $u_{ij}^{i'j'}$ and the factor $\beta_{ij}^{i'j'}$ have, respectively, the following expressions:

$$u_{ij}^{i'j'} = \begin{cases} \sqrt{\dfrac{2\,E_{ij}^{i'j'}}{\mu_{ij}}} & \text{if } E_{ij}^{i'j'} > 0, \\ 0 & \text{if } E_{ij}^{i'j'} \leq 0, \end{cases} \tag{16}$$

$$\beta_{ij}^{i'j'} = \sqrt{1 - \frac{2\,E_{ij}^{i'j'}}{\mu_{ij} u^2}}, \quad i \in \mathcal{I}_{\mathcal{S}},\, (i', j, j') \in \mathcal{C}_i^{\text{in}}, \tag{17}$$

where $E_{ij}^{i'j'} = (E_{i'} + E_{j'}) - (E_i + E_j)$.

III. Numerical method

Numerical solutions to Eq. (3) are sought for 1D flows. After introducing the two Cartesian reference frames for the position and the velocity ($\mathcal{C}_{\mathcal{R}} = (O_{\mathcal{R}}; x, y, z)$ and $\mathcal{C}_{\mathcal{V}} = (O_{\mathcal{V}}; v_x, v_y, v_z)$, respectively) and after taking the flow direction coincident with that of the x axis, Eq. (3) simplifies to:

$$\frac{\partial f_i}{\partial t} + v_x \frac{\partial f_i}{\partial x} = \sum_{j \in \mathcal{I}_{\mathcal{S}}} Q_{ij}(\mathbf{v}) + \sum_{(i',j,j') \in \mathcal{C}_i^{\text{in}}} Q_{ij}^{i'j'}(\mathbf{v}), \quad i \in \mathcal{I}_{\mathcal{S}}, \tag{18}$$

where v_x in Eq. (18) is the projection of the velocity vector $\mathbf{v} = (v_x, v_y, v_z)$ along the x axis, $v_x = \mathbf{v} \cdot \mathbf{i}_x$. In this particular case, the velocity distribution function f_i satisfying Eq. (18) depends on the spatial coordinate x, the velocity components v_x, v_y, v_z and the time t. Hence, one may write $f_i = f_i(x, \mathbf{v}, t) = f_i(x, v_x, v_y, v_z, t)$.

In order to obtain numerical solutions to Eq. (3), the following steps must be taken:

1. Discretization of the the phase-space,
2. Choice of a time-marching technique,
3. Device of a computational algorithm allowing both for an efficient evaluation of each single collision operator in Eq. (18) and conservation of mass, momentum and energy during collisions.

All the items of the previous list are described in detail in the Sects. III.A - III.C.

III.A. Phase-space discretization

The velocity domain is discretized by considering points falling inside a cube centered at the origin $O_{\mathcal{V}}$ and with side semi-length L_v:

$$\mathcal{V} = \{\mathbf{v} = (v_x, v_y, v_z) \in \mathcal{C}_{\mathcal{V}} \quad | v_x \in [-L_v, L_v), \quad v_y \in [-L_v, L_v), \quad v_z \in [-L_v, L_v)\}. \tag{19}$$

The individual velocity nodes belonging to the set $\mathcal{V}$ in Eq. (19) are obtained as follows. Let Δv be the velocity mesh spacing, defined as:

$$\Delta v = \frac{2\,L_v}{N_v}, \tag{20}$$

where N_v is the number of velocity nodes along the v_x, v_y and v_z directions, let $\mathbf{k} = (\mathrm{k}_x, \mathrm{k}_y, \mathrm{k}_z)$ be the vector of indices corresponding to the velocity node $\mathbf{v}_{\mathbf{k}} = (v_{\mathrm{k}_x}, v_{\mathrm{k}_y}, v_{\mathrm{k}_z})$ and let $\mathcal{I}_{\mathcal{V}}$ be the set $\mathcal{I}_{\mathcal{V}} = \{0, \ldots, N_v - 1\}$. The Cartesian components of the velocity node $\mathbf{v}_{\mathbf{k}}$ belonging to the set $\mathcal{V}$ in Eq. (19) are then computed as:

$$v_{\mathrm{k}_x} = -L_v + \mathrm{k}_x\,\Delta v, \quad \mathrm{k}_x \in \mathcal{I}_{\mathcal{V}}, \tag{21}$$

$$v_{\mathrm{k}_y} = -L_v + \mathrm{k}_y\,\Delta v, \quad \mathrm{k}_y \in \mathcal{I}_{\mathcal{V}}, \tag{22}$$

$$v_{\mathrm{k}_z} = -L_v + \mathrm{k}_z\,\Delta v, \quad \mathrm{k}_z \in \mathcal{I}_{\mathcal{V}}. \tag{23}$$

Eqs. (21) - (23) can also be cast into a vector equation:

$$\mathbf{v}_{\mathbf{k}} = -L_v \left(\mathbf{i}_{v_x} + \mathbf{i}_{v_y} + \mathbf{i}_{v_z}\right) + \mathbf{k}\,\Delta v, \quad \mathbf{k} = (\mathrm{k}_x, \mathrm{k}_z, \mathrm{k}_y) \in \mathcal{I}_{\mathcal{V}}^3. \tag{24}$$

In Eq. (24) the vectors $\mathbf{i}_{v_x}$, $\mathbf{i}_{v_y}$ and $\mathbf{i}_{v_z}$ are, respectively, the unit vectors of the v_x, v_y and v_z axes of the Cartesian velocity frame $\mathcal{C}_{\mathcal{V}}$, and the set $\mathcal{I}_{\mathcal{V}}^3$ is defined as $\mathcal{I}_{\mathcal{V}}^3 = \mathcal{I}_{\mathcal{V}} \times \mathcal{I}_{\mathcal{V}} \times \mathcal{I}_{\mathcal{V}}$. As mentioned in Sect. II, the numerical method used for the evaluation of each single collision operator of Eq. (18) makes use of the Fourier transform of the former (given in Eqs. (10) - (13)). This is the reason why a Fourier velocity space (associated to the *physical* velocity space described above) is introduced and discretized. The discretization of the former is performed as follows. Once a Cartesian reference frame $\mathcal{C}_{\mathcal{V}_\mathcal{F}} = (O_{\mathcal{V}_\mathcal{F}}; \zeta_x, \zeta_y, \zeta_z)$ introduced in the Fourier velocity space, the points falling inside a cube centered at the origin $O_{\mathcal{V}_\mathcal{F}}$ and with semi-length L_η are selected:

$$\mathcal{V}_F = \{\boldsymbol{\zeta} = (\zeta_x, \zeta_y, \zeta_z) \in \mathcal{C}_{\mathcal{V}_\mathcal{F}} \quad | \zeta_x \in [-L_\eta, L_\eta), \quad \zeta_y \in [-L_\eta, L_\eta), \ \zeta_z \in [-L_\eta, L_\eta)\}, \tag{25}$$

The Fourier velocity nodes belonging to the set $\mathcal{V}_F$ in Eq. (25) are obtained by applying the same methodology as used for the *physical* velocity nodes (Eq. (24)). Let $\Delta\eta$ be the Fourier velocity domain mesh spacing, defined as:

$$\Delta\eta = \frac{2\,L_\eta}{N_v}, \tag{26}$$

and let $\boldsymbol{\varepsilon} = (\varepsilon_x, \varepsilon_y, \varepsilon_z)$ be the vector of indices corresponding to the Fourier velocity node $\boldsymbol{\zeta}_{\boldsymbol{\varepsilon}} = (\zeta_{\varepsilon_x}, \zeta_{\varepsilon_y}, \zeta_{\varepsilon_z})$. The Cartesian components of the Fourier velocity node $\boldsymbol{\zeta}_{\boldsymbol{\varepsilon}}$ belonging to the set $\mathcal{V}_F$ in Eq. (25) are then computed as:

$$\zeta_{\varepsilon_x} = -L_\eta + \varepsilon_x\,\Delta\eta, \quad \varepsilon_x \in \mathcal{I}_{\mathcal{V}}, \tag{27}$$

$$\zeta_{\varepsilon_y} = -L_\eta + \varepsilon_y\,\Delta\eta, \quad \varepsilon_y \in \mathcal{I}_{\mathcal{V}}, \tag{28}$$

$$\zeta_{\varepsilon_z} = -L_\eta + \varepsilon_z\,\Delta\eta, \quad \varepsilon_z \in \mathcal{I}_{\mathcal{V}}. \tag{29}$$

As already done for the *physical* velocity nodes, the individual Cartesian components for the Fourier velocity node $\boldsymbol{\zeta}_{\boldsymbol{\varepsilon}}$ in Eqs. (27) - (29) can be cast into a vector equation:

$$\boldsymbol{\zeta}_{\boldsymbol{\varepsilon}} = -L_\eta \left(\mathbf{i}_{\zeta_x} + \mathbf{i}_{\zeta_y} + \mathbf{i}_{\zeta_z}\right) + \boldsymbol{\varepsilon}\Delta v, \quad \boldsymbol{\varepsilon} = (\varepsilon_x, \varepsilon_y, \varepsilon_y) \in \mathcal{I}_{\mathcal{V}}^3, \tag{30}$$

where the vectors $\mathbf{i}_{\zeta_x}$, $\mathbf{i}_{\zeta_y}$ and $\mathbf{i}_{\zeta_z}$ are, respectively, the unit vectors of the ζ_x, ζ_y and ζ_z axes of the Cartesian Fourier velocity space $\mathcal{C}_{\mathcal{V}_\mathcal{F}}$.

In the present work, the semi-length L_v and the number of nodes N_v along each direction of the *physical* velocity domain are provided as input parameters to the spectral-Lagrangian Boltzmann solver. The velocity domain mesh spacing Δv is then computed according to Eq. (20). The semi-length L_η and the mesh spacing $\Delta\eta$ of the Fourier velocity domain are found by imposing in Eq. (26) the following condition:

$$\Delta\eta\,\Delta v = \frac{2\,\pi}{N_v}. \tag{31}$$

The substitution of the expressions for Δv and $\Delta\eta$ (Eq. (20) and Eq. (26), respectively) in Eq. (31) leads to:

$$L_\eta = \frac{\pi N_v}{2\,L_v}. \tag{32}$$

In Eq. (32), the semi-length L_η is completely determined from the input parameters (N_v and L_v). Once L_η computed, the Fourier velocity domain mesh spacing $\Delta\eta$ is then found from Eq. (26). The choice of a uniform mesh along each direction of the velocity domains and of the condition provided by Eq. (31) are due to the use of the Fast-Fourier-Transform (FFT) algorithm [7] for the evaluation of the Fourier and the inverse Fourier transforms (see Sect. III.B and App. A).

The Cartesian position domain $\mathcal{C}_\mathcal{R}$ is discretized by considering points belonging to the following subset $\mathcal{X}$ of the x axis:

$$\mathcal{X} = \left\{(x, 0, 0) \in \mathcal{C}_\mathcal{R} \quad | x \in [-L_x^-, L_x^+]\right\}, \tag{33}$$

where the quantities L_x^- and L_x^- in Eq. (33) are both taken as positive. A finite volume grid can be defined based on Eq. (33). Let N_x be the number of nodes in the position domain, s be the index corresponding to the node x_s in the discretized position domain and $\mathcal{I}_\mathcal{X}$ the set $\mathcal{I}_\mathcal{X} = \{0, \ldots, N_x - 2\}$. The centroid location x_s^c and the volume Δx_s of the cell s (volume) contained between the nodes s and s + 1 are computed as:

$$x_\mathrm{s}^c = \frac{1}{2}(x_{\mathrm{s}+1} + x_\mathrm{s}), \tag{34}$$

$$\Delta x_\mathrm{s} = x_{\mathrm{s}+1} - x_\mathrm{s}, \quad \mathrm{s} \in \mathcal{I}_\mathcal{X}. \tag{35}$$

The time domain is discretized as follows. Let N_T be the number time-steps, Δt_n the time-step value associated to the time-level t^n and $\mathcal{I}_\mathcal{T}$ the set $\mathcal{I}_\mathcal{T} = \{0, \ldots, N_T\}$. The set of nodes of the discretized time-domain is then:

$$\mathcal{T} = \left\{ t^n = \sum_{m \leq n} \Delta t_m \ \in \Re \ | n, m \in \mathcal{I}_\mathcal{T} \right\}. \tag{36}$$

For sake of later convenience, it is useful to introduce the following compact notation for the value of the velocity distribution function of the species i at the point $(x_\mathrm{s}, \mathbf{v}_\mathbf{k})$ of the discretized phase space at the time-level value t^n:

$$f_{i\,\mathrm{s}\,\mathbf{k}}^{\ n} = f_i(x_\mathrm{s}, \mathbf{v}_\mathbf{k}, t^n) = f_i(x_\mathrm{s}, v_{\mathrm{k}_x}, v_{\mathrm{k}_y}, v_{\mathrm{k}_z}, t^n), \quad \mathbf{v}_\mathbf{k} \in \mathcal{V},\, x_\mathrm{s} \in \mathcal{X},\, t^n \in \mathcal{T}. \tag{37}$$

III.B. Time marching technique - Operator splitting

The operator splitting approach is used for obtaining numerical solutions to Eq. (18). The solution at the time level $n+1$ is obtained based on that at the time level n by combining updates computed by considering separately the advection and the homogeneous contributions to Eq. (18). In the advection (or transport) problem, the collisionless Boltzmann equation is considred:

$$\frac{\partial f_i}{\partial t} + v_x \frac{\partial f_i}{\partial x} = 0, \quad i \in \mathcal{I}_\mathcal{S}, \tag{38}$$

and the solution update $f_{i\,\mathrm{s}\,\mathbf{k}}^{\ n^*} = \mathcal{A}_{\Delta t^\mathcal{A}}(f_{i\,\mathrm{s}\,\mathbf{k}}^{\ n})$ is computed (with $\mathcal{A}$ being the advection problem operator and $\Delta t^\mathcal{A}$ the related time-step). In the homogeneous (or collision) problem, one considers the space homogeneous Boltzmann equation:

$$\frac{\partial f_i}{\partial t} = \sum_{j \in \mathcal{I}_\mathcal{S}} Q_{\,ij}(\mathbf{v}) + \sum_{(i',j,j') \in \mathcal{C}_i^{\mathrm{in}}} Q_{ij}^{\,i'j'}(\mathbf{v}), \quad i \in \mathcal{I}_\mathcal{S}, \tag{39}$$

and the update $f_{i\,\mathrm{s}\,\mathbf{k}}^{\ n+1} = \mathcal{H}_{\Delta t^\mathcal{H}}(f_{i\,\mathrm{s}\,\mathbf{k}}^{\ n^*})$ is computed (with $\mathcal{H}$ being the homogeneous problem operator and $\Delta t^\mathcal{H}$ the related time-step). The solution at time level $n+1$ is obtained by combining the results of the two operators $\mathcal{A}_{\Delta t^\mathcal{A}}$ and $\mathcal{H}_{\Delta t^\mathcal{H}}$ as:

$$f_{i\,\mathrm{s}\,\mathbf{k}}^{\ n+1} = \mathcal{H}_{\Delta t^\mathcal{H}}\left(\mathcal{A}_{\Delta t^\mathcal{A}}(f_{i\,\mathrm{s}\,\mathbf{k}}^{\ n})\right), \quad i \in \mathcal{I}_\mathcal{S},\, s \in \mathcal{I}_\mathcal{X},\, \mathbf{k} \in \mathcal{I}_\mathcal{V}^3,\, n \in \mathcal{I}_\mathcal{T}. \tag{40}$$

Advection problem

The advection problem (Eq. (38)) is solved by means of the Finite volume method. Since the velocity and space coordinates are independent, Eq. (38) represents a first order linear advection equation for which robust numerical methods have been devised [15]. The application of the Finite volume method to Eq. (38) leads to the following semi-discrete equation for the discretized distribution function:

$$\Delta x_\mathrm{s} \frac{\partial f_{i\,\mathrm{s}\,\mathbf{k}}}{\partial t} + \mathcal{F}_{i\,\mathrm{s}+1/2\,\mathbf{k}} - \mathcal{F}_{i\,\mathrm{s}-1/2\,\mathbf{k}} = 0, \quad i \in \mathcal{I}_\mathcal{S},\, s \in \mathcal{I}_\mathcal{X},\, \mathbf{k} \in \mathcal{I}_\mathcal{V}^3, \tag{41}$$

where Δx_s is the volume of the cell s (Eq. (35)). The numerical flux $\mathcal{F}_{i\,\mathrm{s}+1/2\,\mathbf{k}}$ in Eq. (41) is evaluated by means of a second order slope-limited upwind scheme [15]:

$$\mathcal{F}_{i\,\mathrm{s}+1/2\,\mathbf{k}} = a_k^+ \, f_{i\,\mathrm{s}\,\mathbf{k}}^{\mathrm{L}} + a_k^- \, f_{i\,\mathrm{s}+1\,\mathbf{k}}^{\mathrm{R}}, \quad i \in \mathcal{I}_\mathcal{S},\, s \in \mathcal{I}_\mathcal{X},\, \mathbf{k} \in \mathcal{I}_\mathcal{V}^3, \tag{42}$$

where a_k^+ and a_k^- are, respectively, the positive and negative wave speeds:

$$a_k^+ = \max(v_{\mathrm{k}_x}, 0), \tag{43}$$

$$a_k^- = \min(v_{\mathrm{k}_x}, 0), \quad \mathrm{k}_x \in \mathcal{I}_\mathcal{V}, \tag{44}$$

and $f_{i\,\mathrm{s}\,\mathbf{k}}^{\mathrm{L}}$ and $f_{i\,\mathrm{s}+1\,\mathbf{k}}^{\mathrm{R}}$ are the reconstructed values of the distribution function at the left and right sides, respectively, of the interface s+1/2 between the cells s and $s+1$. The reconstructed values of the distribution functions ($f_{i\,\mathrm{s}\,\mathbf{k}}^{\mathrm{L}}$ and $f_{i\,\mathrm{s}+1\,\mathbf{k}}^{\mathrm{R}}$) are obtained by means of a limited MUSCL [15] reconstruction:

$$f_{i\,\mathrm{s}\,\mathbf{k}}^{\mathrm{L}} = f_{i\,\mathrm{s}\,\mathbf{k}} + \frac{1}{2}\phi(r^{\mathrm{L}}) \left(f_{i\,\mathrm{s}\,\mathbf{k}} - f_{i\,\mathrm{s}-1\,\mathbf{k}}\right), \tag{45}$$

$$f_{i\,\mathrm{s}+1\,\mathbf{k}}^{\mathrm{R}} = f_{i\,\mathrm{s}+1\,\mathbf{k}} - \frac{1}{2}\phi(r^{\mathrm{R}}) \left(f_{i\,\mathrm{s}+2\,\mathbf{k}} - f_{i\,\mathrm{s}+1\,\mathbf{k}}\right), \quad i \in \mathcal{I}_\mathcal{S},\, s \in \mathcal{I}_\mathcal{X},\, \mathbf{k} \in \mathcal{I}_\mathcal{V}^3. \tag{46}$$

In Eqs. (45) - (45), ϕ is a slope limiter function (such as those proposed by van Albada, van Leer *et al* [15]) and r^{L} and r^{R} are, respectively, the left and right ratios of consecutive differences:

$$r^{\mathrm{L}} = \frac{f_{i\,\mathrm{s}+1\,\mathbf{k}} - f_{i\,\mathrm{s}\,\mathbf{k}}}{f_{i\,\mathrm{s}\,\mathbf{k}} - f_{i\,\mathrm{s}-1\,\mathbf{k}}}, \tag{47}$$

$$r^{\mathrm{R}} = \frac{f_{i\,\mathrm{s}+1\,\mathbf{k}} - f_{i\,\mathrm{s}\,\mathbf{k}}}{f_{i\,\mathrm{s}+2\,\mathbf{k}} - f_{i\,\mathrm{s}+1\,\mathbf{k}}}, \quad i \in \mathcal{I}_{\mathcal{S}},\, s \in \mathcal{I}_{\mathcal{X}},\, \mathbf{k} \in \mathcal{I}_{\mathcal{V}}^3. \tag{48}$$

For the time integration of Eq. (41), the Forward Euler method is considered:

$$f_{i\,\mathrm{s}\,\mathbf{k}}^{\,n^*} = f_{i\,\mathrm{s}\,\mathbf{k}}^{\,n} - \frac{\Delta t_{\mathbf{k}}^{\mathrm{a}}}{\Delta x_{\mathrm{s}}} \left(\mathcal{F}_{i\,\mathrm{s}+1/2\,\mathbf{k}} - \mathcal{F}_{i\,\mathrm{s}-1/2\,\mathbf{k}} \right), \quad i \in \mathcal{I}_{\mathcal{S}},\, s \in \mathcal{I}_{\mathcal{X}},\, \mathbf{k} \in \mathcal{I}_{\mathcal{V}}^3,\, n \in \mathcal{I}_{\mathcal{T}}. \tag{49}$$

In Eq. (49) the time-step $\Delta t_{\mathbf{k}}^{\mathrm{a}}$ is computed based on the CFL number as $\Delta t_{\mathbf{k}}^{\mathrm{a}} = \Delta x_{\mathrm{s}}\,\mathrm{CFL}/|v_{\mathrm{k}_x}|$. Due to the narrow stability region of the Forward Euler method [15], multi-stage time stepping schemes (such as Runge-Kutta methods) could be considered, since they allow for the use of higher CFL numbers.

Boundary conditions are applied through ghost cells [15].

Homogeneous problem

The homogeneous problem consists in the solution of the following ordinary differential equation at each point of the discretized phase-space:

$$\frac{\partial f_{i\,\mathrm{s}\,\mathbf{k}}}{\partial t} = Q_{\,i\,\mathrm{s}\,\mathbf{k}}, \quad i \in \mathcal{I}_{\mathcal{S}},\, s \in \mathcal{I}_{\mathcal{X}},\, \mathbf{k} \in \mathcal{I}_{\mathcal{V}}^3. \tag{50}$$

In Eq. (50) the quantity $Q_{\,i\,\mathrm{s}\,\mathbf{k}}$ represents the sum of all the collision operators (evaluated at the point $(x_{\mathrm{s}}, \mathbf{v}_{\mathbf{k}})$ of the discretized phase-space) in the Boltzmann equation written for the species i. The application of the Forward Euler method to Eq. (50) leads to the solution value at time level $n+1$ (with the initial value provided by the solution of the advection problem, Eq. (49)):

$$f_{i\,\mathrm{s}\,\mathbf{k}}^{\,n+1} = f_{i\,\mathrm{s}\,\mathbf{k}}^{\,n^*} + \Delta t^{\,\mathrm{c}}\, Q_{i\,\mathrm{s}\,\mathbf{k}}^{\,n^*}, \quad i \in \mathcal{I}_{\mathcal{S}},\, s \in \mathcal{I}_{\mathcal{X}},\, \mathbf{k} \in \mathcal{I}_{\mathcal{V}}^3,\, n \in \mathcal{I}_{\mathcal{T}}. \tag{51}$$

In Eq. (51), the quantity $\Delta t^{\,\mathrm{c}}$ is the collision time-step. The computational algorithm used for the numerical evaluation of each single collision operator entering in $Q_{\,i\,\mathrm{s}\,\mathbf{k}}$ in Eq. (50) is described in Sect. III.C.

III.C. Computational algorithm for the evaluation of the collision operator

For the interaction (whether elastic or inelastic) between the species i and j given by Eq. (1), the following steps are performed (the notation used below refers to an elastic collisional interaction):

1. Compute the Fourier transforms $\hat{f}_{i,j}(\boldsymbol{\zeta}) = \mathcal{F}(f_{i,j}(\mathbf{v})) \;\rightarrow\; O(N_v^3 \log N_v)$.
2. For N_v^3 Fourier velocity nodes compute the Fourier transform of the collision operator $Q_{\,ij}(\mathbf{v})$ by means of the weighted convolution in the Fourier velocity space:

$$\hat{Q}_{\,ij}(\boldsymbol{\zeta}) = \int \hat{f}_i\,(\boldsymbol{\zeta} - \boldsymbol{\xi})\; \hat{f}_j(\boldsymbol{\xi})\, \tilde{G}_{ij}\,(\boldsymbol{\zeta}, \boldsymbol{\xi})\; d\boldsymbol{\xi} \;\rightarrow\; O(N_v^3).$$

3. Compute the inverse Fourier transform $\tilde{Q}_{\,ij}(\mathbf{v}) = \mathcal{F}^{-1}(\hat{Q}_{\,ij}(\boldsymbol{\zeta})) \;\rightarrow\; O(N_v^3 \log N_v)$.
4. For N_v^3 velocity nodes enforce conservation through the solution of a constrained optimization problem:

$$Q_{\,ij}(\mathbf{v}) = \mathrm{Opt}(\tilde{Q}_{\,ij}(\mathbf{v})) \;\rightarrow\; O(N_v^3).$$

The global cost of the algorithm is $O(N_v^6)$ (per interaction) and the last step is performed in order to ensure conservation of mass, momentum and energy during collisions. This approach was originally proposed and formulated by Gamba *et al* in [7] for the case of a pure gas without internal energy. In the present work an extension to mixtures is proposed. Elastic and inelastic collisions are treated separately and the enforcement of conservation of macroscopic moments is imposed through the following constrained optimization problems:

1. Elastic collisions:

$$\mathcal{P}_{\rm el} = \left\{ \min \sum_{i,j \in \mathcal{I}_{\mathcal{S}}} \left|\left| \tilde{\mathbf{Q}}_{ij} - \mathbf{Q}_{ij} \right|\right|_2^2 \, , \; \sum_{i,j \in \mathcal{I}_{\mathcal{S}}} \mathbf{C}_{{\rm el}\, i} \, \mathbf{Q}_{ij} = \mathbf{0}_{N_s+4} \right\}. \tag{52}$$

2. Inelastic collisions:

$$\mathcal{P}_{\rm in} = \left\{ \min \sum_{i \in \mathcal{I}_{\mathcal{S}}} \sum_{(i',j,j') \in \mathcal{C}_i^{\rm in}} \left|\left| \tilde{\mathbf{Q}}_{ij}^{i'j'} - \mathbf{Q}_{ij}^{i'j'} \right|\right|_2^2 \, , \; \sum_{i \in \mathcal{I}_{\mathcal{S}}} \sum_{(i',j,j') \in \mathcal{C}_i^{\rm in}} \mathbf{C}_{{\rm in}\, i} \, \mathbf{Q}_{ij}^{i'j'} = \mathbf{0}_5 \right\}. \tag{53}$$

In Eqs. (52) - (53), the vector $\mathbf{0}_n$ stands for the n-component null vector, the vectors $\tilde{\mathbf{Q}}_{ij}$ and $\tilde{\mathbf{Q}}_{ij}^{i'j'}$ store the values of the collision operators $Q_{ij}(\mathbf{v})$ and $Q_{ij}^{i'j'}(\mathbf{v})$, respectively, on the velocity nodes given by Eq. (24) (after completing the third step of the algorithm), the vectors store $\mathbf{Q}_{ij}$ and $\mathbf{Q}_{ij}^{i'j'}$ the corrected values of the collision operators $Q_{ij}(\mathbf{v})$ and $Q_{ij}^{i'j'}(\mathbf{v})$, respectively, obtained as solution of the two constrained optimization problems (Eqs. (52)-(53)) and the matrices $\mathbf{C}_{{\rm el}\, i}$ and $\mathbf{C}_{{\rm in}\, i}$ are integration matrices. The columns of the former, when expressed for the velocity node $\mathbf{v}_{\mathbf{k}} = (v_{{\rm k}_x}, v_{{\rm k}_y}, v_{{\rm k}_z})$, are given by:

$$(\mathbf{C}_{{\rm el}\, i})_{\mathbf{k}} = \Omega_{\mathbf{k}} \left[\begin{array}{cccc} m_i \, \delta_{il} & m_i \, v_{{\rm k}_x} & m_i \, v_{{\rm k}_y} & m_i \, v_{{\rm k}_z} \end{array} \; \frac{1}{2} m_i \, V_{\mathbf{k}}^2 \right]^{\rm T}, \quad i, l \in \mathcal{I}_{\mathcal{S}}, \tag{54}$$

$$(\mathbf{C}_{{\rm in}\, i})_{\mathbf{k}} = \Omega_{\mathbf{k}} \left[\begin{array}{cccc} m_i & m_i \, v_{{\rm k}_x} & m_i \, v_{{\rm k}_y} & m_i \, v_{{\rm k}_z} \end{array} \; \frac{1}{2} m_i \, V_{\mathbf{k}}^2 + E_i \right]^{\rm T}, \quad i \in \mathcal{I}_{\mathcal{S}}, \tag{55}$$

where δ_{ij} is Kroenecker's delta, $V_{\mathbf{k}}^2 = v_{{\rm k}_x}^2 + v_{{\rm k}_y}^2 + v_{{\rm k}_z}^2$ and $\Omega_{\mathbf{k}} = \Omega_{{\rm k}_x} \Omega_{{\rm k}_y} \Omega_{{\rm k}_z}$ is the integration weight associated to the velocity node $\mathbf{v}_{\mathbf{k}} = (v_{{\rm k}_x}, v_{{\rm k}_y}, v_{{\rm k}_z})$. The structure of the matrices in Eqs. (54) - (55) reflects the fact that there exists a set of $N_s + 4$ collisional invariants for elastic collisions (the single species mass, the global momentum and energy), while, for inelastic collisions, the number of collisional invariants is equal to 5 (the global mass, momentum and energy) [1,2]. It can be shown that the solutions to the above constrained optimization problems (Eqs. (52) - (53)) are:

1. Elastic collisions:

$$\mathbf{Q}_{ij} = \tilde{\mathbf{Q}}_{ij} - \frac{1}{N_s} \mathbf{C}_{{\rm el}\, i}^{\rm T} \left(\sum_{p \in \mathcal{I}_{\mathcal{S}}} \mathbf{C}_{{\rm el}\, p} \, \mathbf{C}_{{\rm el}\, p}^{\rm T} \right)^{-1} \left(\sum_{p,q \in \mathcal{I}_{\mathcal{S}}} \mathbf{C}_{{\rm el}\, p} \tilde{\mathbf{Q}}_{pq} \right), \quad i, j \in \mathcal{I}_{\mathcal{S}}. \tag{56}$$

2. Inelastic collisions:

$$\mathbf{Q}_{ij}^{i'j'} = \tilde{\mathbf{Q}}_{ij}^{i'j'} - \frac{1}{N_{\rm in}} \mathbf{C}_{{\rm in}\, ,i}^{\rm T} \left(\sum_{p \in \mathcal{I}_{\mathcal{S}}} \mathbf{C}_{{\rm in}\, p} \, \mathbf{C}_{{\rm in}\, p}^{\rm T} \right)^{-1} \left(\sum_{p \in \mathcal{I}_{\mathcal{S}}} \sum_{(p',q,q') \in \mathrm{C}_p^{\rm in}} \mathbf{C}_{{\rm in}\, p} \, \tilde{\mathbf{Q}}_{pq}^{p'q'} \right), \quad i \in \mathcal{I}_{\mathcal{S}}, \, (i',j,j') \in \mathcal{C}_i^{\rm in}, \tag{57}$$

with $N_{\rm in} = N_s(N_s^2 - 1)$.

For the details related to the evaluation of the Fourier and inverse Fourier transforms, weighted convolution in the Fourier velocity space and the formal solutions of the constrained optimization problems for elastic and inelastic collisions the reader is referred to App. A, B and C.

IV. Computational results

The numerical method described in detail in Sect. III has been implemented in a parallel C code. Parallelization is performed by means of the OpenMP library [16]. The GSL [17] and FFTW3 [18] libraries are used, respectively, for vector/matrix manipulation and the implementation of the FFT and inverse FFT algorithms.

IV.A. Flow across a normal shock wave in Ar

The gas consists of Ar atoms. Only elastic collisions are accounted for (the excitation of the Ar atom electronic states lying above the ground state is not considered). The Boltzmann equation (Eq. (18)) is solved in the shock wave reference frame and adopting the one-dimensional position domain shown in Fig. 1).

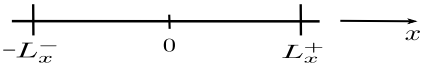

Figure 1: Position domain used for normal shock wave flow calculations.

The flow goes from the left boundary placed at $x = -L_x^-$ to the right one placed at $x = L_x^+$. At these locations, a Maxwellian velocity distribution function corresponding to free-stream and post-shock conditions, respectively, is imposed:

$$f(-L_x^-, \mathbf{v}_\mathbf{k}, t^n) = n_\infty \left(\frac{m}{2\,\pi\,k_\mathrm{B}\,T_\infty}\right)^{3/2} \exp\left(-\frac{m\,||V_\infty\,\mathbf{i}_{v_x} - \mathbf{v}_\mathbf{k}||_2^2}{2\,k_\mathrm{B}\,T_\infty}\right), \tag{58}$$

$$f(L_x^+, \mathbf{v}_\mathbf{k}, t^n) = n_\mathrm{ps} \left(\frac{m}{2\,\pi\,k_\mathrm{B}\,T_\mathrm{ps}}\right)^{3/2} \exp\left(-\frac{m\,||V_\mathrm{ps}\,\mathbf{i}_{v_x} - \mathbf{v}_\mathbf{k}||_2^2}{2\,k_\mathrm{B}\,T_\mathrm{ps}}\right), \quad \forall\,\mathbf{v}_\mathbf{k} \in \mathcal{V},\, \forall\, t^n \in \mathcal{T}. \tag{59}$$

In Eq. (59) (and in what follows) the species index has been dropped for sake of clarity. The sub-scripts ∞ and ps in Eq. (59) refer, respectively, to the free-stream and post-shock conditions. The numerical values of the post-shock number density n_ps, velocity V_ps and temperature T_ps in Eq. (59), are computed by means of the Rankine-Hugoniot jump relations [19]:

$$\frac{\rho_\mathrm{ps}}{\rho_\infty} = \frac{(\gamma+1)\,M_\infty}{(\gamma-1)\,M_\infty + 2}, \tag{60}$$

$$\frac{T_\mathrm{ps}}{T_\infty} = \frac{[(\gamma-1)\,M_\infty]\,[2\,\gamma\,M_\infty - (\gamma-1)]}{(\gamma+1)^2\,M_\infty}, \tag{61}$$

$$\frac{V_\mathrm{ps}}{V_\infty} = \frac{\rho_\infty}{\rho_\mathrm{ps}}, \tag{62}$$

with $\rho_\infty = m\,n_\infty$ and $\rho_\mathrm{ps} = m\,n_\mathrm{ps}$. In Eqs. (60) - (61) the specific heat ratio γ is set to 5/3 (monatomic gas without internal structure) and the free-stream Mach number M_∞ is defined as $M_\infty = V_\infty/\sqrt{\gamma\,k_\mathrm{B}/m\,T_\infty}$.

The free-stream values of the density and the temperature have been set to, respectively, $1 \times 10^{-4}\,\mathrm{kg/m^3}$ and 300 K (corresponding to a free-stream pressure of 6.25 Pa). Three different values of the free-stream Mach number have been considered. The numerical values for the former are provided in Table 1 together with those for the N_v and L_v parameters needed for the velocity space discretization and the post-shock conditions (expressed in terms of density, temperature and velocity) obtained from Eqs. (60) - (62).

Case	M_∞	N_v	L_v [m/s]	ρ_ps [kg/m^3]	T_ps [K]	V_ps [m/s]
1	1.55	24	2200	1.78×10^{-4}	464.32	281.01
2	3.38	32	3700	3.17×10^{-4}	1328.61	344.17
3	6.5	40	6500	3.74×10^{-4}	4222.11	561.43

Table 1: Velocity space discretization parameters and post-shock conditions.

For all the cases given in Table 1, the position domain shown in Fig. 1 has been discretized by considering a uniform mesh of 200 cells ($N_x = 201$) between the locations $x = -0.02$ m and $x = 0.02$ m (corresponding to $L_x^- = L_x^+ = 0.02$ m). The solution is initialized by setting the velocity distribution function equal to the pre-shock Maxwellian (Eq. (58)) for the cells contained within the interval $[-L_x^-, 0]$, while for the remaining part of the discretized position domain the post-shock Maxwellian (Eq. (59)) is used. Numerical solutions have been obtained by means of the operator splitting technique described in Sect. III.B. For the advection (or transport) problem, the CFL number has been set to 0.5 and van Albada's limiter [15] has been used for the limited MUSCL reconstruction. For the solution of the homogeneous (or collision) problem, the collision time-step $\Delta t^{\,\mathrm{c}}$ has been set to 1×10^{-8} s.

Cross-section models

The following isotropic cross-section models have been considered:

- Hard-sphere (HS),
- Variable hard-sphere (VHS),
- Cross-section deduced from the viscosity cross-section computed by assuming a Lennard-Jones interaction potential ($\mu\,\mathrm{LJ}$),
- Cross-section deduced from the viscosity cross-section computed by Phelps *et al* [20] for $\mathrm{Ar}-\mathrm{Ar}$ collisions ($\mu\,\mathrm{PL}$).

For the HS model the collision cross-section σ is constant and is [3]:

$$\sigma = \frac{d^2}{4}, \tag{63}$$

where d is the Ar atom diameter. For the VHS, $\mu\,\mathrm{LJ}$ and $\mu\,\mathrm{PL}$ models the collision cross-section has been expressed as a HS cross-section given in Eq. (63) where the diameter d depends on the relative velocity magnitude u, $d = d(u)$. The functional dependence of the diameter $d = d(u)$ for the various cases has been determined as follows.

For the VHS model, the relative velocity dependent diameter $d(u)$ can be expressed as (see [3] for more details):

$$d(u) = \frac{15}{8}\left[\frac{(\pi\, m\, k_\mathrm{B})^{1/2}(4\, k_\mathrm{B}\,/m)^{\omega-1/2}T_\mathrm{ref}^{\omega}}{\Gamma(9/2-\omega)\,\pi\,\mu_\mathrm{ref}}\right]u^{1/2-\omega}, \tag{64}$$

where T_ref and $\mu_\mathrm{ref} = \mu(T_\mathrm{ref})$ are the reference values for the temperature and the dynamic viscosity, while the coefficient ω enters in the dynamic viscosity law:

$$\mu(T) = \mu_\mathrm{ref}\left(\frac{T}{T_\mathrm{ref}}\right)^{\omega}. \tag{65}$$

The parameters μ_ref, T_ref and ω for the cases given in Table 1 are computed as follows. The value of the reference temperature T_ref is set to the arithmetic average between the free-stream and the post-shock values. The dynamic viscosity law coefficient ω and the reference value for the dynamic viscosity μ_ref are obtained by fitting the data given in [21] for the Ar atom dynamic viscosity with Eq. (65). The numerical values for the parameters μ_ref, T_ref and ω are given in Table 2.

Case	M_∞	ω	μ_ref [Pa s]	T_ref [K]
1	1.55	0.791	2.75×10^{-5}	380
2	3.38	0.716	4.84×10^{-5}	820
3	6.5	0.685	9.72×10^{-5}	2300

Table 2: VHS cross-section model parameters.

For the $\mu\,\mathrm{LJ}$ and $\mu\,\mathrm{PL}$ models the velocity dependent diameter $d(u)$ is obtained based on the viscosity cross-section $\sigma^{\,\mu}$ as follows. The viscosity cross-section $\sigma^{\,\mu}$ is defined as [3]:

$$\sigma^{\,\mu} = 2\,\pi\int_{\chi\in[0,2\pi]}\sigma\,\sin^3\chi\,d\,\chi, \tag{66}$$

where χ is the post-collision scattering angle. The integral in Eq. (66) can be also parameterized in terms of the impact parameter b:

$$\sigma^{\,\mu} = 2\,\pi\int_{b\in[0,+\infty)}(1-\cos^2\chi)\,b\,db. \tag{67}$$

If the cross-section σ can be expressed as a HS cross-section (Eq. (63)) with a velocity dependent diameter $d(u)$, the integrals in Eqs. (66) - (67) for the viscosity cross-section can be computed analytically to give:

$$\sigma^{\mu} = \frac{2}{3}\pi d^{2}(u). \tag{68}$$

Solving Eq. (68) for the velocity dependent diameter $d(u)$ one has:

$$d(u) = \sqrt{\frac{3\,\sigma^{\mu}}{2\,\pi}}. \tag{69}$$

Equation (69) suggests that, given an interaction potential for which the viscosity cross-section (as a function of the relative velocity u) is known, the velocity dependent diameter $d(u)$ can be computed based on Eq. (69).

For the μLJ model, the viscosity cross-section σ^{μ} is computed by means of the integral given in Eq. (67) where the post-collision scattering angle χ is obtained by applying the classical elastic scattering theory [1]:

$$\chi = \pi - 2\,b \int\limits_{r\in[r_{\min},+\infty)} \left[1 - 2\,\phi_{\,\mathrm{eff}}(u,b,r)/(\mu\,u^{2})\right]^{-1/2}\,dr. \tag{70}$$

In Eq. (70) $r_{\min}$ is the distance of closest approach and $\phi_{\,\mathrm{eff}}(u,b,r)$ is an effective potential accounting for a spherically symmetric interaction potential and a centrifugal term, $\phi_{\,\mathrm{eff}}(u,b,r) = \phi(r) + \mu\,u^{2}\,b^{2}/(2\,r^{2})$. The interaction potential $\phi(r)$ is given by the well-known Lennard-Jones form:

$$\phi(r) = 4\,\phi_{0}\left[\left(\frac{r_{0}}{r}\right)^{12} - \left(\frac{r_{0}}{r}\right)^{6}\right]. \tag{71}$$

In the present work, for the constants ϕ_0 and r_0 in Eq. (71) the values $1.7\times10^{-21}\,\mathrm{J}$ and $3.4\times10^{-10}\,\mathrm{m}$ have been respectively adopted. In order to avoid numerical problems due to singularities and possible orbiting, the integrals in Eq. (67) and Eq. (70) are transformed via a variable change suggested in [22]. The numerical integration is then performed by means of a doubly-adaptive quadrature technique provided by the GSL library [17].

For the μPL model, the viscosity cross-section computed by Phelps *et al* [20] for $\mathrm{Ar}-\mathrm{Ar}$ collisions has been used. In the above reference, computations account for quantum effects during collisions by means of the WKB (Wentzel-Kramer-Brillouin) approximation [23] and the following fitted expression for the viscosity cross-section σ^{μ} is provided:

$$\sigma^{\mu} = 1.85\times10^{-19}E_{r}^{-3/20}/\sqrt{1 + (E_r/9)^{7/10} + (E_r/200)^{3/2} + (E_r/1000)^{5/2}}, \tag{72}$$

where $E_r = 1/2\,\mu\,u^{2}$ is the relative kinetic energy expressed in eV.

Evolution of macroscopic moments and velocity distribution function

In order to perform a meaningful comparison with the DSMC method (where shown), the origins of the x axis in the numerical solutions obtained by means of the spectral-Lagrangian Boltzmann solver (SLBS) and the DSMC method have been placed at the point where the normalized density $(\rho(x) - \rho_{\infty})/(\rho_{\,\mathrm{ps}} - \rho_{\infty})$ assumes the value of 0.5.

Figure 2 shows the evolution of the density across the shock wave for the $M_{\infty} = 1.55$ and $M_{\infty} = 3.38$ cases when using the HS and VHS models. As expected [3], the HS solution gives a thin shock wave as compared to the VHS solution. This is due to the unrealistic behavior of the HS model that does not account for an actual decrease of the cross-section when increasing the relative velocity. As a result, the collision rate is overestimated leading to a thinner shock wave. For both the HS and VHS models, the agreement between the SLBS and the DMSC method is excellent, confirming the accuracy of the spectral-Lagrangian method for the Boltzmann equation used in the present work. It is worth to recall that the phase-space discretization (see Sect. III.A) is performed independently of the cross-section model in use (*i.e* the discrete velocity grid is exactly the same for both the HS and VHS models). Very good agreement between the SLBS and the DMSC method is also found for higher-order moments such as the kinetic, parallel and transversal temperatures, the stress tensor (xx-component) and the heat flux vector (x-component). Figures 3 - 5 show the evolution of the aforementioned quantities for the $M_{\infty} = 3.38$ and $M_{\infty} = 6.5$ cases when using the VHS model.

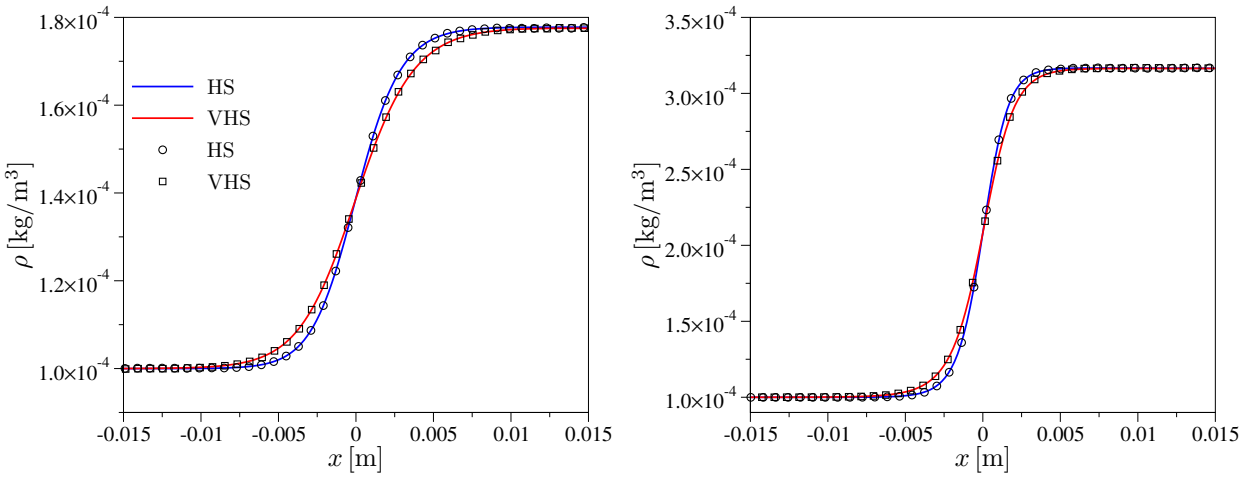

(a) $M_\infty = 1.55$. (b) $M_\infty = 3.38$.

Figure 2: Density for the HS and VHS models (lines SLBS - symbols DSMC).

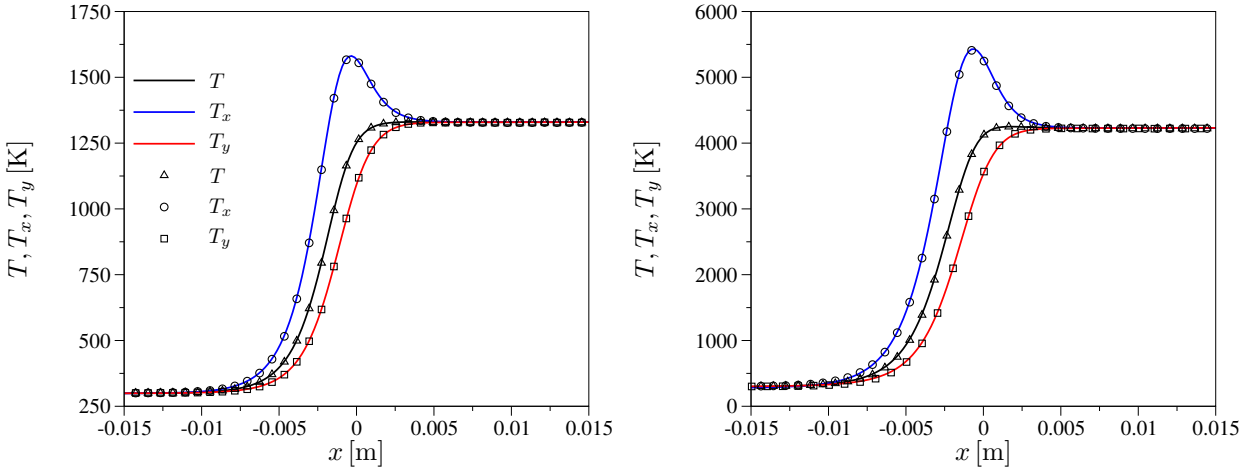

(a) $M_\infty = 3.38$. (b) $M_\infty = 6.5$.

Figure 3: Kinetic, parallel and transversal temperatures for the VHS model (lines SLBS - symbols DSMC).

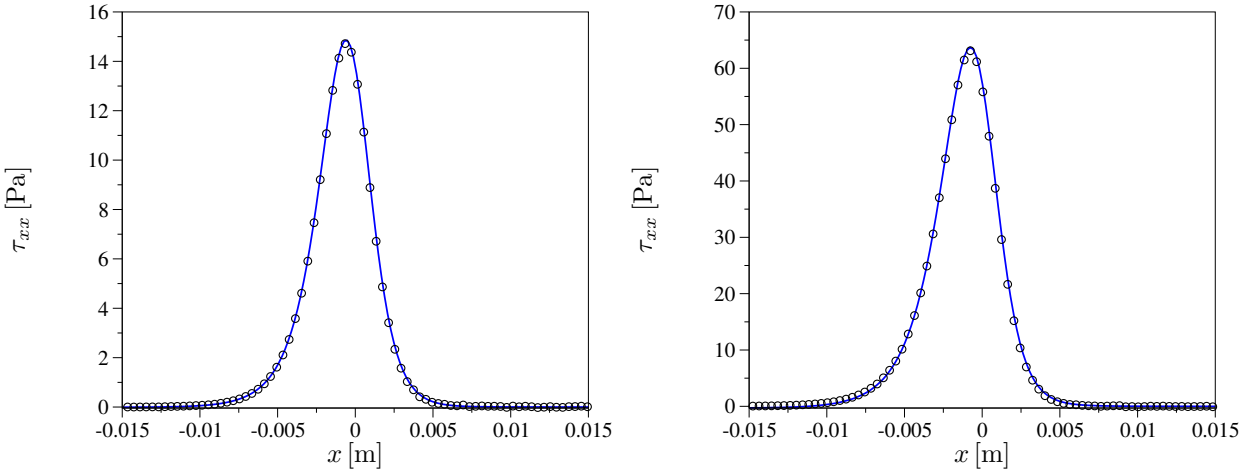

(a) $M_\infty = 3.38$. (b) $M_\infty = 6.5$.

Figure 4: Stress tensor (xx-component) for the VHS model (lines SLBS - symbols DSMC).

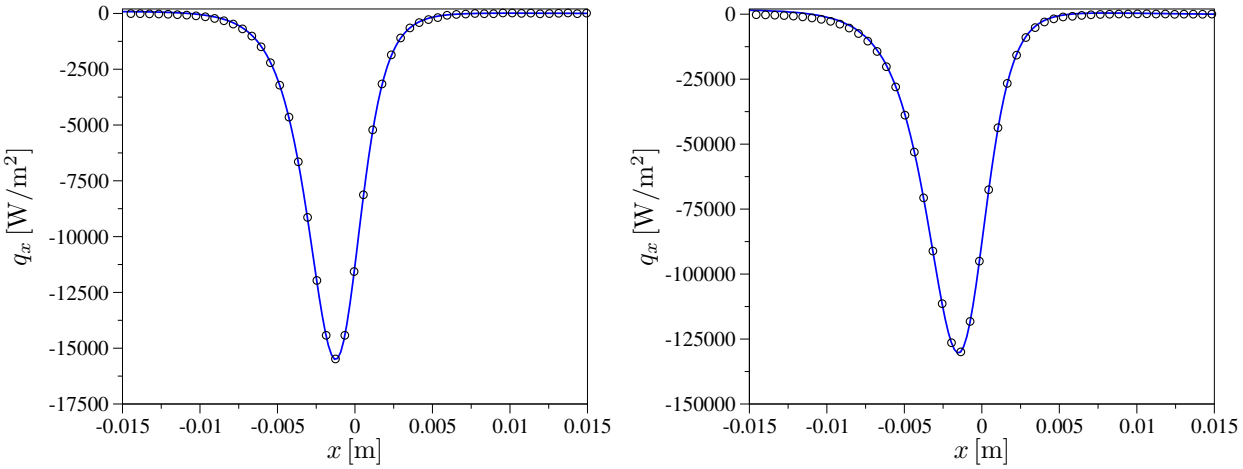

(a) $M_\infty = 3.38$. (b) $M_\infty = 6.5$.

Figure 5: Heat flux vector (x-component) for the VHS model (lines SLBS - symbols DSMC).

Figure 6 shows the evolution across the shock wave of the v_x-axis component of the velocity distribution function for the VHS model ($M_\infty = 6.5$). The evolution from the free-stream to the post-shock Maxwellian occurs through intermediate states where the velocity distribution function experiences severe distortions and assumes a bi-modal shape. The same behavior is observed for the $M_\infty = 3.38$ case (not shown here), though the distortions are less pronounced, while for the $M_\infty = 1.55$ case (not shown here) the velocity distribution function evolves smoothly without any appreciable shape distortion.

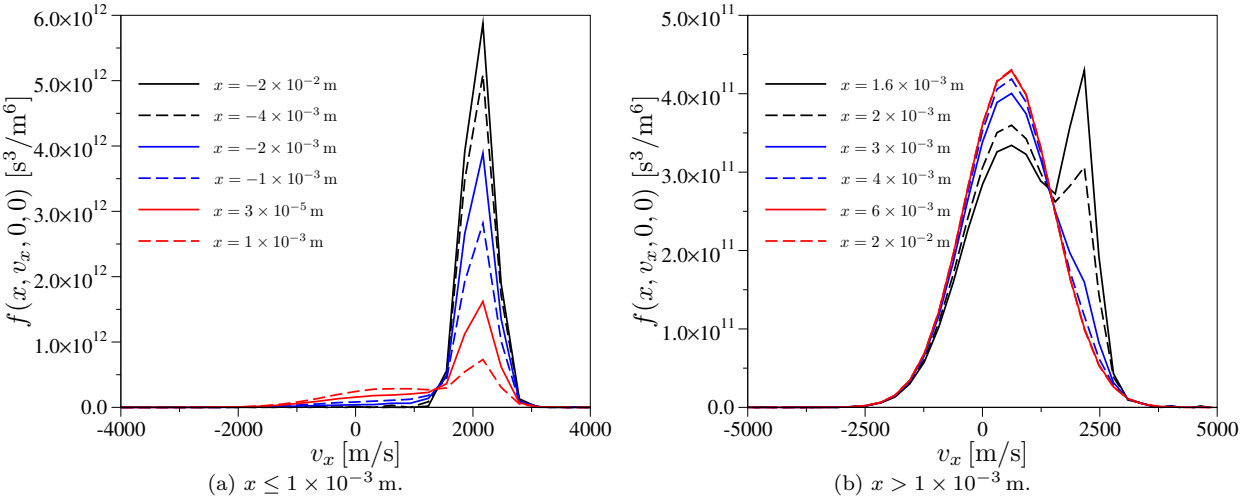

(a) $x \leq 1 \times 10^{-3}$ m. (b) $x > 1 \times 10^{-3}$ m.

Figure 6: Evolution across the shock wave of the v_x-axis component of the velocity distribution function for the VHS model ($M_\infty = 6.5$).

Comparison with Alsmeyer's experimental density profiles

After the accuracy verification through comparison with the DMSC method, the computed density profiles for the $M_\infty = 1.55, 3.38$ and 6.5 cases shown before have been compared with the experiments of Alsmeyer [24] for sake of validation. Figure 7 shows the normalized density $(\rho(x) - \rho_\infty)/(\rho_{\,\mathrm{ps}} - \rho_\infty)$ as a function of the non-dimensional distance x/λ_∞. In obtaining the curves shown in Fig. 7, the free-stream mean free path λ_∞ has been set to the value indicated in the aforementioned reference ($\lambda_\infty = 1.098 \times 10^{-3}$ m), for sake of consistency. For the $M_\infty = 1.55$ and $M_\infty = 3.38$ cases, numerical solutions by means of the SLBS are shown for the VHS, μLJ and μPL cross-section models, while for the $M_\infty = 6.5$ case only the VHS cross-section model has been considered.

The agreement between the computed and experimental density profiles is fairly good, though some discrepancies arise. These can be noticed for all the cases in the initial part of the shock front. In that zone, the average thermal speed of the Ar atoms is quite low due to the moderate value of the gas temperature. In view of that, two colliding atoms will be able to approach each other at a close distance as compared to the case of a high average thermal speed. Hence, the collision dynamics will be strongly influenced by the short-range repulsive forces. From this it can be inferred that, in order to have a good agreement with the experiments in the initial part of the shock front, the cross-section model in use must be based on an interaction potential accounting also for short-range repulsive forces. The VHS cross-section model [3] is based on a purely repulsive interaction and this could explain the systematic disagreement found. On the other hand, the μLJ and μPL cross-section models are based on potentials that account for short-range repulsive forces and show a better agreement with the experiments in the initial part of the shock front.

Before concluding, it is worth to recall that the VHS cross-section model parameters ω, μ_{ref} and T_{ref} (see before) have to be computed for each value of the free-stream Mach number by some appropriate *tuning* approach, if a reasonable agreement with experiments is wished. This is not the case for the μLJ and μPL cross-section models.

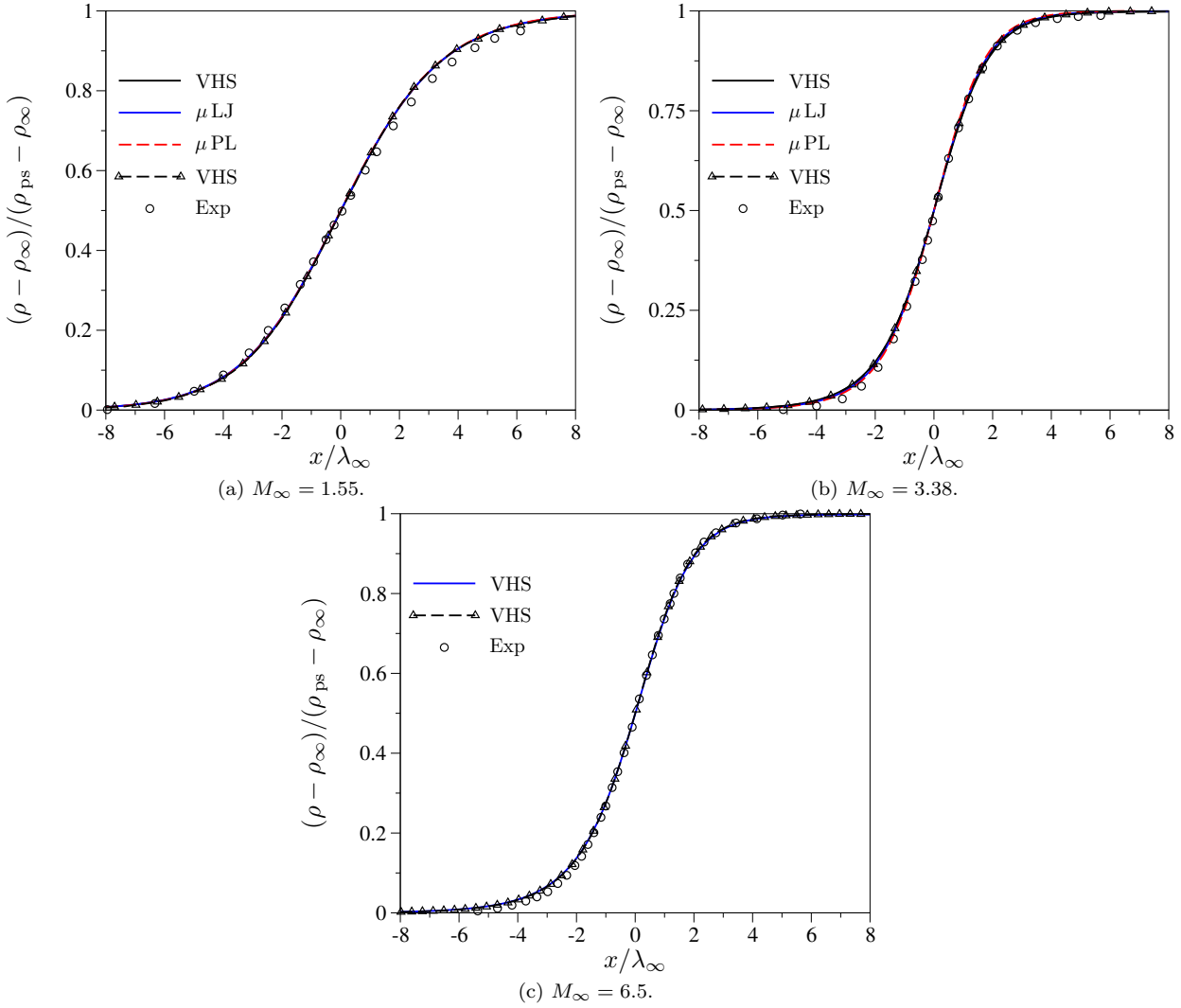

(a) $M_\infty = 1.55$.

(b) $M_\infty = 3.38$.

(c) $M_\infty = 6.5$.

Figure 7: Comparison between computed and experimental density profiles (lines SLBS - lines with symbols DSMC - symbols experiments).

IV.B. Flow across a normal shock wave in a Ne-Ar mixture

After assessing the accuracy of the spectral-Lagrangian method in the case of a pure gas, its extension to mixtures has been tested on the computation of the flow across a normal shock wave in a binary inert gas mixture made of Ne and Ar. A peculiar aspect of this test-case is the species separation occurring within the shock wave. The former is due to the mass difference between the two species [3] with the lighter species experiencing the compression sooner than the heavier one. The free-stream values of density, temperature and Mach number have been set to $1 \times 10^{-4}\,\mathrm{kg/m^3}$, 300 K and 2, respectively. The mass fractions of Ne and Ar have been set to 0.34 and 0.66, respectively, while for the parameters N_v and L_v the values 22 and 2500 m/s, respectively, have been used (the other numerical simulation parameters are the same as that of Sect. IV.A). The HS collision model (Eq. 63) has been used and the numerical values for the species mass and diameter have been taken from [3]. The post-shock conditions are always computed by means of the Rankine-Hugoniot jump relations (Eqs. (60) - (62)) and the solution initialized in the same manner as done in Sect. IV.A for the pure gas case.

Evolution of macroscopic moments and velocity distribution functions

Figure 8 shows the species hydrodynamic velocities, diffusion velocities and mass fractions across the shock wave. The Ne (whose mass is lower than that of Ar) experiences the compression within the shock sooner that the Ar does (as it can be seen from the velocity variation).

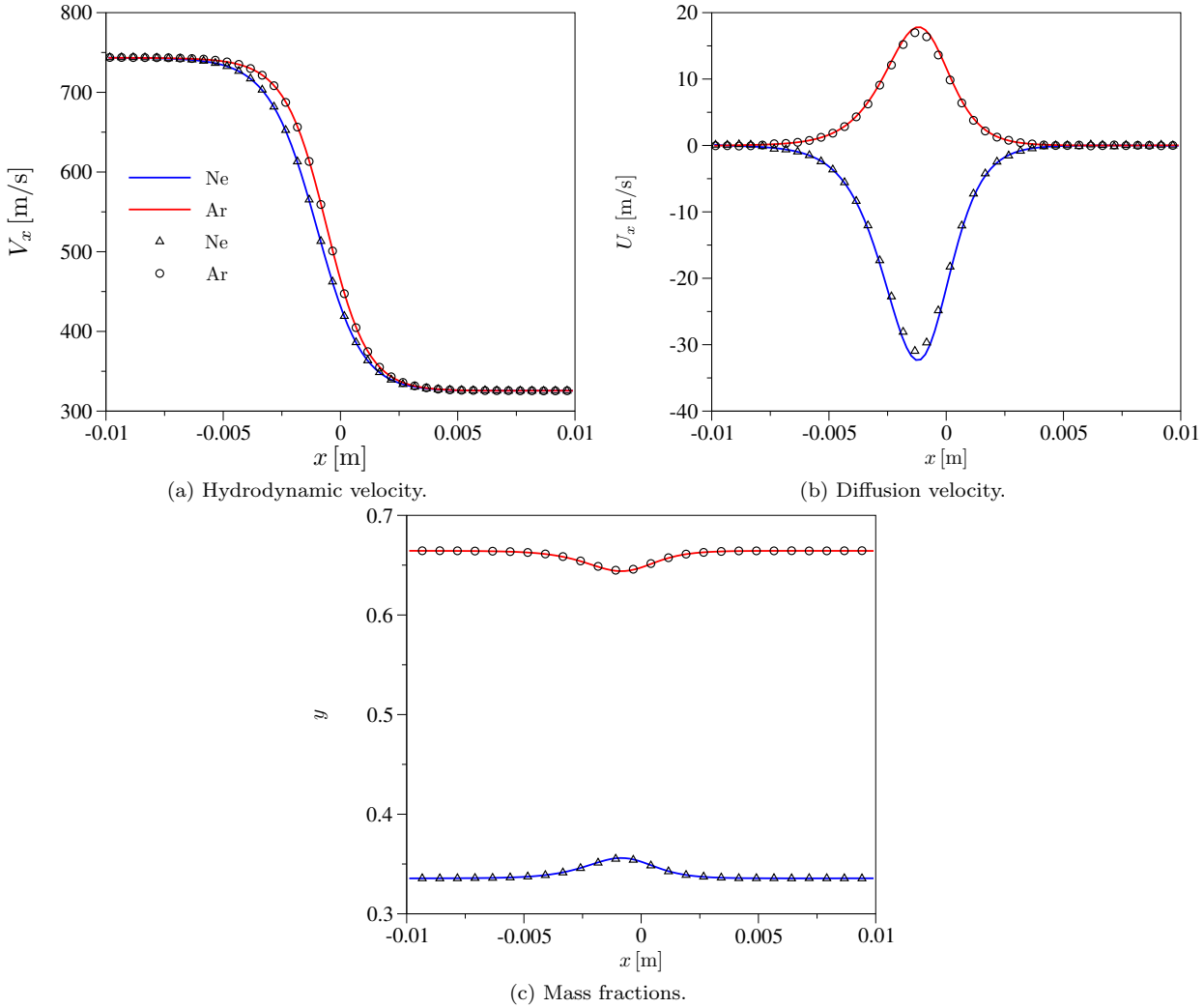

(a) Hydrodynamic velocity.

(b) Diffusion velocity.

(c) Mass fractions.

Figure 8: Species hydrodynamic velocities, diffusion velocities and mass fractions (lines SLBS - symbols DSMC).

This induces an accumulation of Ne atoms in the front part of the shock wave leading, in turn, to a local chemical composition variation. This effect progressively disappears while the flow approaches the post-shock equilibrium state (where no species separation exists) and the chemical composition assumes the same value as that of the free-stream. The species separation can also be appreciated from Fig. showing the species kinetic and parallel temperatures. For each species, the parallel temperature shows the same behavior as that of the pure gas case with the local maximum being more pronounced for the heavier species (Ar). The comparison with the DSMC results is again excellent.

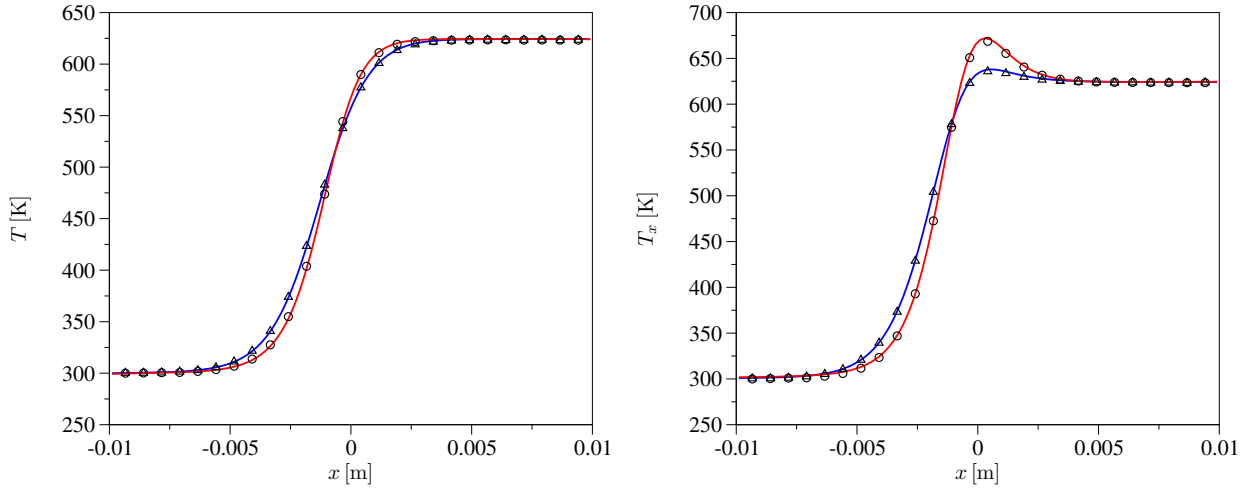

(a) Kinetic temperature. (b) Parallel temperature.

Figure 9: Species kinetic and parallel temperatures (lines SLBS - symbols DSMC).

Figure 10 shows the evolution across the shock wave of the v_x-axis component of the species velocity distribution function. Due to the low value of the free-stream Mach number, small deviation from a Maxwellian shape are observed.

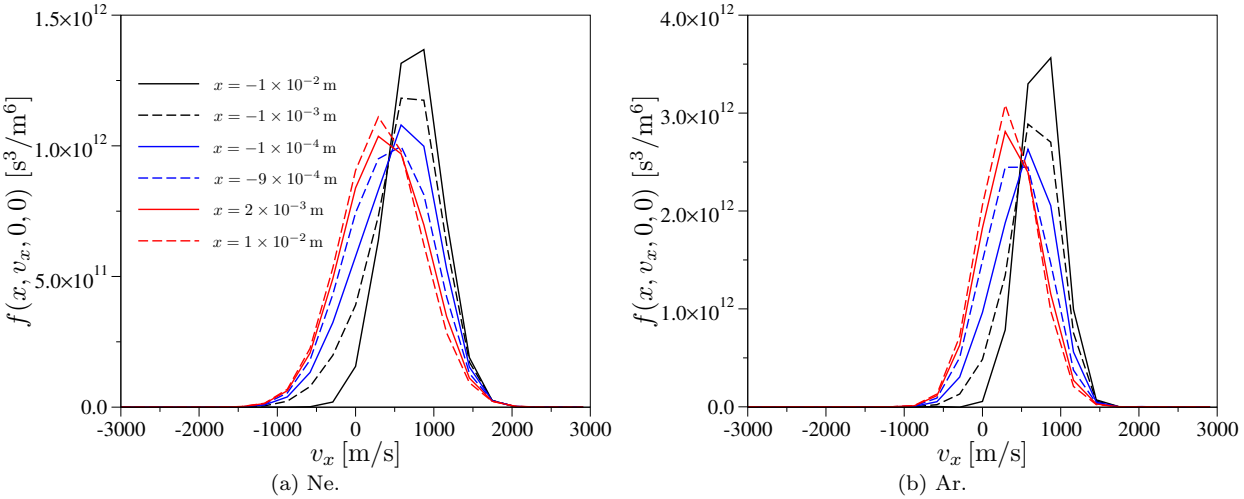

(a) Ne. (b) Ar.

Figure 10: Evolution across the shock wave of the v_x-axis component of the species velocity distribution functions.

V. Conclusions

An existing spectral-Lagrangian deterministic method for the Boltzmann equation for a pure gas has been extended in order to deal with gas mixtures and account for more realistic collision cross-section models. Based on that, a computational tool has been written and numerical solutions have been obtained for the

flow across normal shock waves of pure gases and mixtures. The accuracy of the spectral-Lagrangian method has been verified through comparison with the DSMC method showing very good agreement. For the pure gas case, the density profiles have been compared with experimental measurements. A fairly good agreement has been observed, allowing for a partial validation of the developed computational tool. Future work will focus on internal energy excitation (already accounted for in the formulation) and investigation of alternative phase-space discretization methods (such as momentum space discretization).

Research of A. M., E. T. and T. E. M. is sponsored by the European Research Council Starting Grant #259354, research of J. R. H. is sponsored by the NSF Grant #DMS − 0636586 and research of I. M. G. is sponsored by the NSF Grants #DMS − 1109625 and #DMS − 1107465.

A. Numerical evaluation of the Fourier and inverse Fourier transforms

Let $g = g(\mathbf{v})$ be a function of the velocity $\mathbf{v}$ and let $\hat{h} = \hat{h}(\boldsymbol{\zeta})$ be a function of the Fourier variable $\boldsymbol{\zeta}$. According to the definitions introduced in Sect. II.C, the Fourier transform of the function g and the inverse Fourier transform of the function $\hat{h}$ are:

$$\hat{g}(\boldsymbol{\zeta}) = \frac{1}{\left(\sqrt{2\,\pi}\right)^3} \int\limits_{\mathbf{v}\in\Re^3} \exp\left(-\imath\,\boldsymbol{\zeta}\cdot\mathbf{v}\right)\, g(\mathbf{v})\, d\mathbf{v}, \quad \boldsymbol{\zeta}\in\Re^3, \tag{73}$$

$$h(\mathbf{v}) = \frac{1}{\left(\sqrt{2\,\pi}\right)^3} \int\limits_{\boldsymbol{\zeta}\in\Re^3} \exp\left(\imath\,\boldsymbol{\zeta}\cdot\mathbf{v}\right)\, \hat{h}(\boldsymbol{\zeta})\, d\boldsymbol{\zeta}, \quad \mathbf{v}\in\Re^3. \tag{74}$$

The integrals in Eqs. (73) - (74) must be replaced with discrete sums because of the discretization of the velocity space introduced in Sect. III.A.

Let $\boldsymbol{\Omega}_{\mathbf{k}} = (\Omega_{\mathrm{k}_x}, \Omega_{\mathrm{k}_y}, \Omega_{\mathrm{k}_z})$ be the vector integration weights associated to the discrete velocity node $\mathbf{v}_{\mathbf{k}} = (v_{\mathrm{k}_x}, v_{\mathrm{k}_y}, v_{\mathrm{k}_z})$ and let $\boldsymbol{\Omega}_{\boldsymbol{\varepsilon}} = (\Omega_{\varepsilon_x}, \Omega_{\varepsilon_y}, \Omega_{\varepsilon_z})$ be the vector of integration weights associated to the discrete Fourier velocity node $\boldsymbol{\zeta}_{\boldsymbol{\varepsilon}} = (\zeta_{\varepsilon_x}, \zeta_{\varepsilon_y}, \zeta_{\varepsilon_z})$. The substitution of the Eqs. (21) - (23) and Eqs. (27) - (29) for $\mathbf{v}_{\mathbf{k}}$ and $\boldsymbol{\zeta}_{\boldsymbol{\varepsilon}}$, respectively, in Eqs. (73) - (74) and the replacement of continuous integrals with discrete sums, leads to:

$$\hat{g}(\boldsymbol{\zeta}_{\boldsymbol{\varepsilon}}) = \frac{1}{\left(\sqrt{2\,\pi}\right)^3} \sum_{\mathbf{k}\in\mathcal{I}_{\mathcal{V}}^3} \Omega_{\mathbf{k}} \exp\left(-\imath\,\boldsymbol{\zeta}_{\boldsymbol{\varepsilon}}\cdot\mathbf{v}_{\mathbf{k}}\right)\, g(\mathbf{v}_{\mathbf{k}})\, \Delta v^3, \quad \boldsymbol{\zeta}_{\boldsymbol{\varepsilon}}\in\mathcal{V}_F, \tag{75}$$

$$h(\mathbf{v}_{\mathbf{k}}) = \frac{1}{\left(\sqrt{2\,\pi}\right)^3} \sum_{\boldsymbol{\varepsilon}\in\mathcal{I}_{\mathcal{V}}^3} \Omega_{\boldsymbol{\varepsilon}} \exp\left(\imath\,\boldsymbol{\zeta}_{\boldsymbol{\varepsilon}}\cdot\mathbf{v}_{\mathbf{k}}\right)\, \hat{h}(\boldsymbol{\zeta}_{\boldsymbol{\varepsilon}})\, \Delta\eta^3, \quad \mathbf{v}_{\mathbf{k}}\in\mathcal{V}, \tag{76}$$

where $\Omega_{\mathbf{k}} = \Omega_{\mathrm{k}_x}\Omega_{\mathrm{k}_y}\Omega_{\mathrm{k}_z}$, $\Omega_{\boldsymbol{\varepsilon}} = \Omega_{\varepsilon_x}\Omega_{\varepsilon_y}\Omega_{\varepsilon_z}$. The expansion of the dot product $\boldsymbol{\zeta}_{\boldsymbol{\varepsilon}}\cdot\mathbf{v}_{\mathbf{k}}$ in Eqs. (75)-(76) reads:

$$\boldsymbol{\zeta}_{\boldsymbol{\varepsilon}}\cdot\mathbf{v}_{\mathbf{k}} = (-L_v + \mathrm{k}_x\Delta v)(-L_\eta + \varepsilon_x\Delta\eta) + (-L_v + \mathrm{k}_y\Delta v)(-L_\eta + \varepsilon_y\Delta\eta) + (-L_v + \mathrm{k}_z\Delta v)(-L_\eta + \varepsilon_z\Delta\eta). \tag{77}$$

After some algebraic manipulation, Eq. (77) can be written as:

$$\boldsymbol{\zeta}_{\boldsymbol{\varepsilon}}\cdot\mathbf{v}_{\mathbf{k}} = 3L_vL_\eta - L_v\Delta\eta\,(\varepsilon_x+\varepsilon_y+\varepsilon_z) - L_\eta\Delta v\,(\mathrm{k}_x+\mathrm{k}_y+\mathrm{k}_z) + \frac{2\,\pi}{N_v}(\mathbf{k}\cdot\boldsymbol{\varepsilon}). \tag{78}$$

In obtaining Eq. (78), the relation $\Delta v\Delta\eta = 2\,\pi/N_v$ (Eq. (31)) has been used. The substitution of Eq. (78) in Eqs. (75) - (76) gives:

$$\hat{g}(\boldsymbol{\zeta}_{\boldsymbol{\varepsilon}}) = \frac{\exp\left[-\imath\,\alpha(\boldsymbol{\varepsilon})\right]}{\left(\sqrt{2\,\pi}\right)^3} \sum_{\mathbf{k}\in\mathcal{I}_{\mathcal{V}}^3} g^*(\mathbf{v}_{\mathbf{k}}) \exp\left(-\imath\,\frac{2\,\pi}{N_v}\mathbf{k}\cdot\boldsymbol{\varepsilon}\right), \quad \boldsymbol{\zeta}_{\boldsymbol{\varepsilon}}\in\mathcal{V}_F, \tag{79}$$

$$h(\mathbf{v}_{\mathbf{k}}) = \frac{\exp\left[\imath\,\beta(\mathbf{k})\right]}{\left(\sqrt{2\,\pi}\right)^3} \sum_{\boldsymbol{\varepsilon}\in\mathcal{I}_{\mathcal{V}}^3} \hat{h^*}(\boldsymbol{\zeta}_{\boldsymbol{\varepsilon}}) \exp\left(\imath\,\frac{2\,\pi}{N_v}(\mathbf{k}\cdot\boldsymbol{\varepsilon}\right), \quad \mathbf{v}_{\mathbf{k}}\in\mathcal{V}. \tag{80}$$

The arguments $\alpha(\boldsymbol{\varepsilon})$ and $\beta(\mathbf{k})$ of the exponentials in front of the sums in Eqs. (79) - (80) are:

$$\alpha(\boldsymbol{\varepsilon}) = L_v\left[(L_\eta - \varepsilon_x\Delta\eta) + (L_\eta - \varepsilon_y\Delta\eta) + (L_\eta - \varepsilon_z\Delta\eta)\right], \quad \boldsymbol{\varepsilon}\in\mathcal{I}_{\mathcal{V}}^3, \tag{81}$$

$$\beta(\mathbf{k}) = L_\eta\left[(L_v - \mathrm{k}_x\Delta v) + (L_v - \mathrm{k}_y\Delta v) + (L_v - \mathrm{k}_z\Delta v)\right], \quad \mathbf{k}\in\mathcal{I}_{\mathcal{V}}^3, \tag{82}$$

while the functions $g^*(\mathbf{v}_\mathbf{k})$ and $\hat{h^*}(\boldsymbol{\zeta}_{\boldsymbol{\varepsilon}})$ have the following expressions:

$$g^*(\mathbf{v}_\mathbf{k}) = \Omega_\mathbf{k}\, g(\mathbf{v}_\mathbf{k}) \exp\left[\imath\, L_\eta \Delta v (\mathrm{k}_x + \mathrm{k}_y + \mathrm{k}_z)\right] \Delta v^3, \quad \mathbf{v}_\mathbf{k} \in \mathcal{V}, \tag{83}$$

$$\hat{h^*}(\boldsymbol{\zeta}_{\boldsymbol{\varepsilon}}) = \Omega_{\boldsymbol{\varepsilon}}\, \hat{h}(\boldsymbol{\zeta}_{\boldsymbol{\varepsilon}}) \exp\left[-\imath\, L_v \Delta \eta (\varepsilon_x + \varepsilon_y + \varepsilon_z)\right] \Delta \eta^3, \quad \boldsymbol{\zeta}_{\boldsymbol{\varepsilon}} \in \mathcal{V}_F. \tag{84}$$

The two sums in Eqs. (79) - (80) correspond to the definitions of the Fast-Fourier-Transform (FFT) and inverse Fast-Fourier-Transform (FFT^{-1} of inverse FFT) of a function (with no scaling):

$$\mathrm{FFT}(g^*)(\boldsymbol{\zeta}_{\boldsymbol{\varepsilon}}) = \sum_{\mathbf{k} \in \mathcal{I}_\mathcal{V}^3} g^*(\mathbf{v}_\mathbf{k}) \exp\left(-\imath\, \frac{2\,\pi}{N_v} \mathbf{k} \cdot \boldsymbol{\varepsilon}\right), \quad \boldsymbol{\zeta}_{\boldsymbol{\varepsilon}} \in \mathcal{V}_F, \tag{85}$$

$$\mathrm{FFT}^{-1}(\hat{h^*})(\mathbf{v}_\mathbf{k}) = \sum_{\boldsymbol{\varepsilon} \in \mathcal{I}_\mathcal{V}^3} \hat{h^*}(\boldsymbol{\zeta}_{\boldsymbol{\varepsilon}}) \exp\left(\imath\, \frac{2\,\pi}{N_v} \mathbf{k} \cdot \boldsymbol{\varepsilon}\right) \quad \mathbf{v}_\mathbf{k} \in \mathcal{V}. \tag{86}$$

The above concept suggests the use of the following algorithm for an efficient computation of the Fourier and the inverse Fourier transforms:

1. Given the discrete values of the function g (or $\hat{h}$), the function g^* (or $\hat{h^*}$) is evaluated by means of Eq. (83) (or Eq. (84)).
2. The FFT of g^* (or the inverse FFT of $\hat{h^*}$) is computed by means of Eq. (85) (or Eq. (86)).
3. The result obtained is substituted in Eq. (79)) (or Eq. (80)).

In the present work, the computation of the FFT and the inverse FFT of functions is performed by means of the FFTW3 library (Fastest Fourier Transform in the West) [18].

B. Numerical evaluation of the weighted convolution

In view of the discretization of the velocity space introduced in Sect. III.A, the continuous integrals in the weighted convolutions (Eqs. (10) - (13)) must be replaced with discrete sums. Let $\boldsymbol{\kappa} = (\kappa_x, \kappa_y, \kappa_z)$ and $\boldsymbol{\Omega}_{\boldsymbol{\kappa}} = (\Omega_{\kappa_x}, \Omega_{\kappa_y}, \Omega_{\kappa_z})$ be, respectively, the vector of indices and the vector integration weights associated to the Fourier velocity node $\boldsymbol{\xi}_{\boldsymbol{\kappa}}$. If one refers to the the case of an elastic collisional interaction between the species i and j (for the inelastic case the only thing that changes is the convolution weight), the following expression can be written for the Fourier transform of the collision operator $Q_{ij}(\mathbf{v})$ evaluated at the Fourier velocity node $\boldsymbol{\zeta}_{\boldsymbol{\varepsilon}}$:

$$\hat{Q}_{ij}(\boldsymbol{\zeta}_{\boldsymbol{\varepsilon}}) = \frac{1}{\left(\sqrt{2\,\pi}\right)^3} \sum_{\boldsymbol{\kappa} \in \mathcal{I}^*_{\boldsymbol{\kappa}}} \Omega_{\boldsymbol{\kappa}} \hat{f}_i\left(\boldsymbol{\zeta}_{\boldsymbol{\varepsilon}} - \boldsymbol{\xi}_{\boldsymbol{\kappa}}\right) \hat{f}_j(\boldsymbol{\xi}_{\boldsymbol{\kappa}})\, \tilde{G}_{ij}\left(\boldsymbol{\zeta}_{\boldsymbol{\varepsilon}}, \boldsymbol{\xi}_{\boldsymbol{\kappa}}\right) \Delta \eta^3, \quad i, j \in \mathcal{I}_\mathcal{S}. \tag{87}$$

In Eq. (87), the quantity $\Omega_{\boldsymbol{\kappa}} = \Omega_{\kappa_x} \Omega_{\kappa_y} \Omega_{\kappa_z}$ is the integration weight associated to the Fourier velocity node $\boldsymbol{\xi}_{\boldsymbol{\kappa}}$, while the set $\mathcal{I}^*_{\boldsymbol{\kappa}}$ reads:

$$\mathcal{I}^*_{\boldsymbol{\kappa}} = (\kappa_x^-, \kappa_x^+) \times (\kappa_y^-, \kappa_y^+) \times (\kappa_z^-, \kappa_z^+). \tag{88}$$

In Eq. (88), the $-$ and the $+$ upper-scripts are used to indicate, respectively, the lower and the upper limits for the indices κ_x, κ_y and κ_z associated to the Fourier velocity node $\boldsymbol{\xi}_{\boldsymbol{\kappa}}$ and are computed based on the following relations:

$$\kappa_s^- = \begin{cases} 0 & \text{if } \varepsilon_s < N_v/2, \\ \varepsilon_s - N_v/2 + 1 & \text{if } \varepsilon_s \geq N_v/2, \end{cases} \tag{89}$$

$$\kappa_s^+ = \begin{cases} \varepsilon_s + N_v/2 - 1 & \text{if } \varepsilon_s < N_v/2, \\ N_v & \text{if } \varepsilon_s \geq N_v/2, \quad s \in \{x, y, z\}. \end{cases} \tag{90}$$

The introduction of the above lower and upper limits on the κ_x, κ_y and κ_z indices is equivalent to set to zero the function $\hat{f}_i$ in the discrete sum given in Eq. (87) when its argument $(\boldsymbol{\zeta}_{\boldsymbol{\varepsilon}} - \boldsymbol{\xi}_{\boldsymbol{\kappa}})$ goes beyond the limits of the discrete Fourier velocity space.

C. Formal solution of the constrained optimization problems

C.A. Elastic collisions

For the problem $\mathcal{P}_{\rm el}$ in Eq. (52) the objective function (or Lagrangian) is:

$$\mathcal{L}_{\rm el} = \sum_{\mathbf{k}\in\mathcal{I}_{\mathcal{V}}^3}\sum_{i,j\in\mathcal{I}_{\mathcal{S}}} \left|\left| \tilde{Q}_{ij}^{(\mathbf{k})} - Q_{ij}^{(\mathbf{k})} \right|\right|_2^2 + \boldsymbol{\lambda}_{\rm el}^{\rm T} \sum_{i,j\in\mathcal{I}_{\mathcal{S}}} \mathbf{C}_{{\rm el}\,i}\,\mathbf{Q}_{ij}. \tag{91}$$

In Eq. (91) the quantity $\boldsymbol{\lambda}_{\rm el}$ is the vector (whose number of components is N_s+4) of Lagrange multipliers for the problem $\mathcal{P}_{\rm el}$, while the symbol T stands for the transpose operator. The solution to $\mathcal{P}_{\rm el}$ is given by the stationary points of the Lagrangian $\mathcal{L}_{\rm el}$. These are found by imposing:

$$\frac{\partial \mathcal{L}_{\rm el}}{\partial Q_{ij}^{(\mathbf{k})}} = 0, \quad \mathbf{k} = (\mathrm{k}_x, \mathrm{k}_y, \mathrm{k}_z) \in \mathcal{I}_{\mathcal{V}}^3, \tag{92}$$

$$\frac{\partial \mathcal{L}_{\rm el}}{\partial \lambda_{\rm el}^{(l)}} = 0, \quad l \in \mathcal{I}_{\rm el}, \tag{93}$$

where $\lambda_{\rm el}^{(l)}$ in Eq. (93) is the l-th component of the vector $\boldsymbol{\lambda}_{\rm el}$ and $\mathcal{I}_{\rm el}$ is an index set associated to the elastic collisional invariants and defined as $\mathcal{I}_{\rm el} = \{1, \ldots, N_s+4\}$. The application of Eqs. (92) - (93) gives:

$$\mathbf{Q}_{ij} = \tilde{\mathbf{Q}}_{ij} - \frac{1}{2}\mathbf{C}_{{\rm el}\,i}^{\rm T}\,\boldsymbol{\lambda}_{\rm el}, \tag{94}$$

$$\sum_{i,j\in\mathcal{I}_{\mathcal{S}}} \mathbf{C}_{{\rm el}\,i}\,\mathbf{Q}_{ij} = \mathbf{0}_{N_s+4}. \tag{95}$$

The left-multiplication of Eq. (94) by $\mathbf{C}_{{\rm el}\,i}$ leads to:

$$\mathbf{C}_{{\rm el}\,i}\,\mathbf{Q}_{ij} = \mathbf{C}_{{\rm el}\,i}\,\tilde{\mathbf{Q}}_{ij} - \frac{1}{2}\mathbf{C}_{{\rm el}\,i}\,\mathbf{C}_{{\rm el}\,i}^{\rm T}\,\boldsymbol{\lambda}_{\rm el}. \tag{96}$$

Summing Eq. (96) over the i and j indices belonging to the set $\mathcal{I}_{\mathcal{S}}$ one obtains:

$$\sum_{i,j\in\mathcal{I}_{\mathcal{S}}} \mathbf{C}_{{\rm el}\,i}\,\mathbf{Q}_{ij} = \sum_{i,j\in\mathcal{I}_{\mathcal{S}}} \mathbf{C}_{{\rm el}\,i}\,\tilde{\mathbf{Q}}_{ij} - \frac{N_s}{2}\left(\sum_{i\in\mathcal{I}_{\mathcal{S}}} \mathbf{C}_{{\rm el}\,i}\,\mathbf{C}_{{\rm el}\,i}^{\rm T}\right), \tag{97}$$

that, in view of Eq. (95), becomes:

$$\mathbf{0}_{N_s+4} = \sum_{i,j\in\mathcal{I}_{\mathcal{S}}} \mathbf{C}_{{\rm el}\,i}\,\tilde{\mathbf{Q}}_{ij} - \frac{N_s}{2}\left(\sum_{i\in\mathcal{I}_{\mathcal{S}}} \mathbf{C}_{{\rm el}\,i}\,\mathbf{C}_{{\rm el}\,i}^{\rm T}\right)\boldsymbol{\lambda}_{\rm el}. \tag{98}$$

Eq. (98) can be solved for the Lagrange multiplier vector $\boldsymbol{\lambda}_{\rm el}$:

$$\boldsymbol{\lambda}_{\rm el} = \frac{2}{N_s}\left(\sum_{i\in\mathcal{I}_{\mathcal{S}}} \mathbf{C}_{{\rm el}\,i}\,\mathbf{C}_{{\rm el}\,i}^{\rm T}\right)^{-1}\left(\sum_{i,j\in\mathcal{I}_{\mathcal{S}}} \mathbf{C}_{{\rm el}\,i}\,\tilde{\mathbf{Q}}_{ij}\right). \tag{99}$$

The substitution of Eq. (99) in Eq. (94) gives:

$$\mathbf{Q}_{ij} = \tilde{\mathbf{Q}}_{ij} - \frac{1}{N_s}\mathbf{C}_{{\rm el}\,i}^{\rm T}\left(\sum_{p\in\mathcal{I}_{\mathcal{S}}} \mathbf{C}_{{\rm el}\,p}\,\mathbf{C}_{{\rm el}\,p}^{\rm T}\right)^{-1}\left(\sum_{p,q\in\mathcal{I}_{\mathcal{S}}} \mathbf{C}_{{\rm el}\,p}\,\tilde{\mathbf{Q}}_{pq}\right). \tag{100}$$

In Eq. (100) the original i and j dummy indices in the two sums (coming from Eq. (99)) have been replaced, respectively, with the dummy indices p and q for sake of clarity. Eq. (100) reduces to the result obtained in [7] for a pure gas ($N_s = 1$):

$$\mathbf{Q} = \tilde{\mathbf{Q}} - \mathbf{C}_{\rm el}^{\rm T}\left(\mathbf{C}_{\rm el}\,\mathbf{C}_{\rm el}^{\rm T}\right)^{-1}\mathbf{C}_{\rm el}\tilde{\mathbf{Q}}, \tag{101}$$

where the species subscripts have been omitted.

C.B. Inelastic collisions

For the problem $\mathcal{P}_{\text{in}}$ in Eq. (53) the objective function (or Lagrangian) is:

$$\mathcal{L}_{\text{in}} = \sum_{\mathbf{k}\in\mathcal{I}_{\mathcal{V}}^{3}} \sum_{i\in\mathcal{I}_{\mathcal{S}}} \sum_{(i',j,j')\in\mathcal{C}_{i}^{\text{in}}} \left|\left| \tilde{Q}_{ij}^{i'j'\,(\mathbf{k})} - Q_{ij}^{i'j'\,(\mathbf{k})} \right|\right|_{2}^{2} + \boldsymbol{\lambda}_{\text{in}}^{\text{T}} \sum_{i\in\mathcal{I}_{\mathcal{S}}} \sum_{(i',j,j')\in\mathcal{C}_{i}^{\text{in}}} \mathbf{C}_{\text{in}\,i}\,\mathbf{Q}_{ij}^{i'j'}. \tag{102}$$

In Eq. (102) the quantity $\boldsymbol{\lambda}_{\text{in}}$ is the vector (with 5 components) of Lagrange multipliers for the problem $\mathcal{P}_{\text{in}}$. The solution to $\mathcal{P}_{\text{in}}$ is always found by seeking for the stationary points of the Lagrangian $\mathcal{L}_{\text{in}}$, that is::

$$\frac{\partial\mathcal{L}_{\text{in}}}{\partial Q_{ij}^{i'j'\,(\mathbf{k})}} = 0, \quad \mathbf{k} = (\mathrm{k}_x, \mathrm{k}_y, \mathrm{k}_z) \in \mathcal{I}_{\mathcal{V}}^{3}, \tag{103}$$

$$\frac{\partial\mathcal{L}_{\text{in}}}{\partial\lambda_{\text{in}}^{(\nu)}} = 0, \quad \nu \in \mathcal{I}_{\text{in}}, \tag{104}$$

where $\lambda_{\text{in}}^{(\nu)}$ in Eq. (104) is the ν-th component of the vector $\boldsymbol{\lambda}_{\text{in}}$ and $\mathcal{I}_{\text{in}}$ is an index set associated to the inelastic collisional invariants and defined as $\mathcal{I}_{\text{in}} = \{1, 2, 3, 4, 5\}$. The application of Eqs. (103) - (104) gives:

$$\mathbf{Q}_{ij}^{i'j'} = \tilde{\mathbf{Q}}_{ij}^{i'j'} - \frac{1}{2}\mathbf{C}_{\text{in}\,,i}^{\text{T}}\,\boldsymbol{\lambda}_{\text{in}}, \tag{105}$$

$$\sum_{i\in\mathcal{I}_{\mathcal{S}}} \sum_{(i',j,j')\in\mathcal{C}_{i}^{\text{in}}} \mathbf{C}_{\text{in}\,i}\,\mathbf{Q}_{ij}^{i'j'} = \mathbf{0}_{5}. \tag{106}$$

The left-multiplication of Eq. (105) by $\mathbf{C}_{\text{in}\,i}$ leads to:

$$\mathbf{C}_{\text{in}\,i}\,\mathbf{Q}_{ij}^{i'j'} = \mathbf{C}_{\text{in}\,i}\,\tilde{\mathbf{Q}}_{ij}^{i'j'} - \frac{1}{2}\mathbf{C}_{\text{in}\,i}\,\mathbf{C}_{\text{in}\,,i}^{\text{T}}\,\boldsymbol{\lambda}_{\text{in}}. \tag{107}$$

Summing Eq. (96) over all the ordered triplets (i', j, j') belonging to the set $\mathcal{C}_{i}^{\text{in}}$ one obtains:

$$\sum_{(i',j,j')\in\mathcal{C}_{i}^{\text{in}}} \mathbf{C}_{\text{in}\,i}\,\mathbf{Q}_{ij}^{i'j'} = \sum_{(i',j,j')\in\mathcal{C}_{i}^{\text{in}}} \mathbf{C}_{\text{in}\,i}\,\tilde{\mathbf{Q}}_{ij}^{i'j'} - \frac{N_{\text{in}}}{2}\mathbf{C}_{\text{in}\,i}\,\mathbf{C}_{\text{in}\,,i}^{\text{T}}\,\boldsymbol{\lambda}_{\text{in}}, \tag{108}$$

where the quantity N_{in} in Eq. (108) is:

$$N_{\text{in}} = \sum_{(i',j,j')\in\mathcal{C}_{i}^{\text{in}}} 1 = N_s\left(N_s^2 - 1\right), \tag{109}$$

The sum of Eq. (108) over the i indices belonging to the set $\mathcal{I}_{\mathcal{S}}$ gives:

$$\sum_{i\in\mathcal{I}_{\mathcal{S}}} \sum_{(i',j,j')\in\mathcal{C}_{i}^{\text{in}}} \mathbf{C}_{\text{in}\,i}\,\mathbf{Q}_{ij}^{i'j'} = \sum_{i\in\mathcal{I}_{\mathcal{S}}} \sum_{(i',j,j')\in\mathcal{C}_{i}^{\text{in}}} \mathbf{C}_{\text{in}\,i}\,\tilde{\mathbf{Q}}_{ij}^{i'j'} - \frac{N_{\text{in}}}{2}\left(\sum_{i\in\mathcal{I}_{\mathcal{S}}} \mathbf{C}_{\text{in}\,i}\,\mathbf{C}_{\text{in}\,,i}^{\text{T}}\right)\boldsymbol{\lambda}_{\text{in}}. \tag{110}$$

In view of Eq. (106), Eq. (110) becomes:

$$\mathbf{0}_{5} = \sum_{i\in\mathcal{I}_{\mathcal{S}}} \sum_{(i',j,j')\in\mathcal{C}_{i}^{\text{in}}} \mathbf{C}_{\text{in}\,i}\,\tilde{\mathbf{Q}}_{ij}^{i'j'} - \frac{N_{\text{in}}}{2}\left(\sum_{i\in\mathcal{I}_{\mathcal{S}}} \mathbf{C}_{\text{in}\,i}\,\mathbf{C}_{\text{in}\,,i}^{\text{T}}\right)\boldsymbol{\lambda}_{\text{in}} \tag{111}$$

Eq. (111) can be solved for the Lagrange multiplier vector $\boldsymbol{\lambda}_{\text{in}}$:

$$\boldsymbol{\lambda}_{\text{in}} = \frac{2}{N_{\text{in}}}\left(\sum_{i\in\mathcal{I}_{\mathcal{S}}} \mathbf{C}_{\text{in}\,i}\,\mathbf{C}_{\text{in}\,,i}^{\text{T}}\right)^{-1}\left(\sum_{i\in\mathcal{I}_{\mathcal{S}}} \sum_{(i',j,j')\in\mathcal{C}_{i}^{\text{in}}} \mathbf{C}_{\text{in}\,i}\,\tilde{\mathbf{Q}}_{ij}^{i'j'}\right). \tag{112}$$

The substitution of Eq. (111) in Eq. (105) leads to:

$$\mathbf{Q}_{ij}^{i'j'} = \tilde{\mathbf{Q}}_{ij}^{i'j'} - \frac{1}{N_{\text{in}}}\mathbf{C}_{\text{in}\,,i}^{\text{T}}\left(\sum_{p\in\mathcal{I}_{\mathcal{S}}} \mathbf{C}_{\text{in}\,p}\,\mathbf{C}_{\text{in}\,p}^{\text{T}}\right)^{-1}\left(\sum_{p\in\mathcal{I}_{\mathcal{S}}} \sum_{(p',q,q')\in\mathcal{C}_{p}^{\text{in}}} \mathbf{C}_{\text{in}\,p}\,\tilde{\mathbf{Q}}_{pq}^{p'q'}\right). \tag{113}$$

In Eq. (113) the original i', j and j' dummy indices in the two sums (coming from Eq. (112)) have been replaced, respectively, with the dummy indices p', q and q' for sake of clarity.

References

[1]Ferziger, J. H. and Kaper, H. G., *Mathematical theory of transport processes in gases*, North-Holland Pub. Co., 1972.

[2]Giovangigli, V., *Multicomponent flow modeling*, Birkhäser, 1999.

[3]Bird, G. A., *Molecular gas dynamics and the direct simulation of gas flows*, Clarendon, 1994.

[4]Ivanov, M. K., Kashakovsky, A., Gimelshein, S., Markelov, G., Alexeenko, A., Bondar, Y., Zhukova, G., Nikiforov, S., and Vashenkov, P., "SMILE system for 2D/3D DSMC computations," *Proc. of the 25th Int. Symposium on Rarefied Gas Dynamics*, AIP, 2006.

[5]Tcheremissine, F. G., "Solution of the Boltzmann equation for high-speed flows," *Comput. Math. Math. Phys.*, Vol. 46, No. 2, 2006, pp. 329–343.

[6]Clarke, P. B., Varghese, P. L., and Goldstein, D. B., "A novel discrete velocity method for solving the Boltzmann equation including internal energy and variable grids in velocity space," *Proc. of the 28th Int. Symposium on Rarefied Gas Dynamics*, AIP, 2012.

[7]Gamba, I. M. and Tharkabhushanam, S. H., "Shock and boundary structure formation by spectral-Lagrangian methods for the inhomogeneous Boltzmann transport equation," *J. Comput. Math.*, Vol. 28, No. 4, 2010, pp. 430–460.

[8]Filbet, F. and Russo, G., "High order numerical methods for the space non-homogeneous Boltzmann equation," *J. Comput. Phys.*, Vol. 186, No. 2, 2003, pp. 457–480.

[9]Kobolov, V. I., Arlsanbekov, R. R., Aristov, V. V., Frolova, A. A., and Zabelok, S. A., "Unified solver for rarefied and continuum flows with adaptive mesh refinement," *J. Comput. Phys.*, Vol. 223, No. 2, 2007, pp. 589–608.

[10]Munafò, A., Haack, J. R., Gamba, I. M., and Magin, T. E., "Investigation of nonequilibrium internal energy excitation in shock waves by means of a spectral-lagrangian Boltzmann solver," *Proc. of the 28th Int. Symposium on Rarefied Gas Dynamics*, AIP, 2012.

[11]Magin, T. E., Massot, M., and Graille, B., "Hydrodynamic model for molecular gases in thermal non-equilibrium," *Proc. of the 28th Int. Symposium on Rarefied Gas Dynamics*, AIP, 2012.

[12]Bobylev, A. V., "The method of the Fourier transform in the theory of the Boltzmann equation for Maxwell molecules," *Dokl. Akad. Nauk SSSR*, Vol. 225, No. 6, 1975, pp. 1041–1044, in Russian.

[13]Haack, J. R. and Gamba, I. M., "High-perfomance computing for conservative spectral Boltzmann solvers," *Proc. of the 28th Int. Symposium on Rarefied Gas Dynamics*, AIP, 2012.

[14]Haack, J. R. and Gamba, I. M., "Conservative deterministic spectral Boltzmann-Poisson solver near the Landau limit," *Proc. of the 28th Int. Symposium on Rarefied Gas Dynamics*, AIP, 2012.

[15]Hirsch, C., *Numerical computation of internal and external flows*, Wiley, 1988.

[16]Chapman, B., Jost, G., and van der Pas, R., *Using OpenMP*, MIT press, 2008.

[17]"GSL - GNU Scientific Library," `http://www.gnu.org/software/gsl/`, 2012, [Online; accessed 07-August-2012].

[18]Frigo, M. and Johnson, S. G., "The Design and Implementation of FFTW3," *Proc. of the IEEE*, Vol. 93, No. 2, 2005, pp. 216–231.

[19]Anderson, J. D., *Hypersonic and high temperature gasdynamics*, McGraw-Hill, 1989.

[20]Phelps, A. V., Greene, C. H., and Jr, J. P. B., "Collision cross sections for argon atoms with argon atoms for energies from 0.01 eV to 10 keV," *J. Phys. B*, Vol. 33, No. 16, 2000, pp. 2965–2981.

[21]Svehla, R. A., "Transport Coefficients for the NASA Lewis Chemical Equilibrium Program," NASA TM 4647, 1995.

[22]Magin, T. E., *A Model for Inductive Plasma Wind Tunnels*, Ph.D. thesis, Univesité Libre de Bruxelles, Bruxelles, Belgium, 2004.

[23]Mott, N. F. and Massey, H. S. W., *The Theory of Atomic Collisions*, Oxford University Press, 1987, 3rd edition.

[24]Alsmeyer, H., "Density profiles in argon and nitrogen shock waves measured by the absorption of an electron beam," *J. Fluid Mech.*, Vol. 74, No. 3, 1976, pp. 497–513.